

# MUC18-targeted humanized monoclonal antibody immunePET imaging and patient-derived tumor xenograft visualization

Qian Zhang<sup>1</sup>, Haizhen Du<sup>1</sup>, Xiuli Ma<sup>1</sup>, Song Liu<sup>1</sup>, Xiangxing Kong<sup>1</sup>, Muye Hu<sup>1</sup>, Jing Shi<sup>2</sup>, Yanfang Tang<sup>2</sup>, Shuhui Liu<sup>2</sup>, Xun Meng<sup>2</sup>, Qian Guo<sup>1</sup>, Yan Kong<sup>1</sup>, Jun Guo<sup>1</sup>, Bin Lian<sup>1</sup>, Zhi Yang<sup>1</sup>, and Hua Zhu<sup>1</sup>

<sup>1</sup>Peking University Cancer Hospital

<sup>2</sup>Multitude Therapeutics

August 25, 2024

## Abstract

**Background:** In the context of precision diagnosis for various subtypes of melanoma, identifying biomarkers with clinical translational potential from a molecular standpoint is crucial for a more comprehensive characterization of the disease. MUC18 is highly expressed in both tumor cells and tumor vasculature in major melanoma subtypes and is restricted to normal tissues. **Methods:** A noninvasive imaging approach for MUC18 in melanoma utilizing an immune Positron Emission Tomography (PET) radionuclide-conjugated drug (RDC) with an 89Zr-labeled humanized anti-MUC18 monoclonal antibody (mAb) was developed. A375, Sk-Mel-28, HMVII, and A549 cells and tumor model mice were conducted. Immuno-PET was employed to assess the specificity and targeting of three distinct melanoma cell line-derived xenografts (CDXs) and patient-derived tumor xenografts (PDXs) in immunodeficient mice. **Results:** The developed RDC, named 89Zr-IP150, demonstrated robust in vitro stability and high binding affinity, ensuring reliable and specific PET imaging of small, medium, and large subcutaneous tumors in human melanoma mouse xenotransplantation models. Notably, for the first time, the clinical translational potential of 89Zr-IP150 was successfully validated using a PDX model. **Conclusions:** These findings present a noninvasive, real-time method for the early screening of MUC18 (+) melanoma patients and are important for studying the early-stage biological distribution of MUC18-targeted antibody-drug conjugates (ADCs).

## MUC18-targeted humanized monoclonal antibody immunePET imaging and patient-derived tumor xenograft visualization

Qian Zhang<sup>a, b#</sup>, Haizhen Du<sup>c#</sup>, Xiuli Ma<sup>e#</sup>, Song Liu<sup>b</sup>, Xiangxing Kong<sup>b</sup>, Muye Hu<sup>b</sup>, Jing Shi<sup>d</sup>, Yanfang Tang<sup>d</sup>, Shuhui Liu<sup>d</sup>, Xun Meng<sup>d</sup>, Qian Guo<sup>c</sup>, Yan Kong<sup>c</sup>, Jun Guo<sup>c</sup>, Bin Lian<sup>c\*</sup>, Zhi Yang<sup>a,b\*</sup>, Hua Zhu<sup>a,b\*</sup>

<sup>a</sup> Guizhou University Medicine College, Guizhou Province, Guiyang 550025, China

<sup>b</sup> State Key Laboratory of Holistic Integrative Management of Gastrointestinal Cancers, Beijing Key Laboratory of Carcinogenesis and Translational Research, NMPA Key Laboratory for Research and Evaluation of Radiopharmaceuticals (National Medical Products Administration), Department of Nuclear Medicine, Peking University Cancer Hospital & Institute, No.52 Fucheng Rd, Beijing 100142, China

<sup>c</sup> Department of Renal Cancer and Melanoma, Key Laboratory of Carcinogenesis and Translational Research (Ministry of Education/Beijing), Peking University Cancer Hospital and Institute, No.52 Fucheng Rd, Beijing 100142, China

<sup>d</sup> Multitude Therapeutics, 159 Tianzhou Road, Xuhui District, Shanghai 200030, China

<sup>e</sup> Department of Pathology, Peking University Cancer Hospital and Institute, Beijing, 100142, China

# These authors contributed equally to this work

### Corresponding authors:

\*Bin Lian. E-mail: [lianb608@bjmu.edu.cn](mailto:lianb608@bjmu.edu.cn).

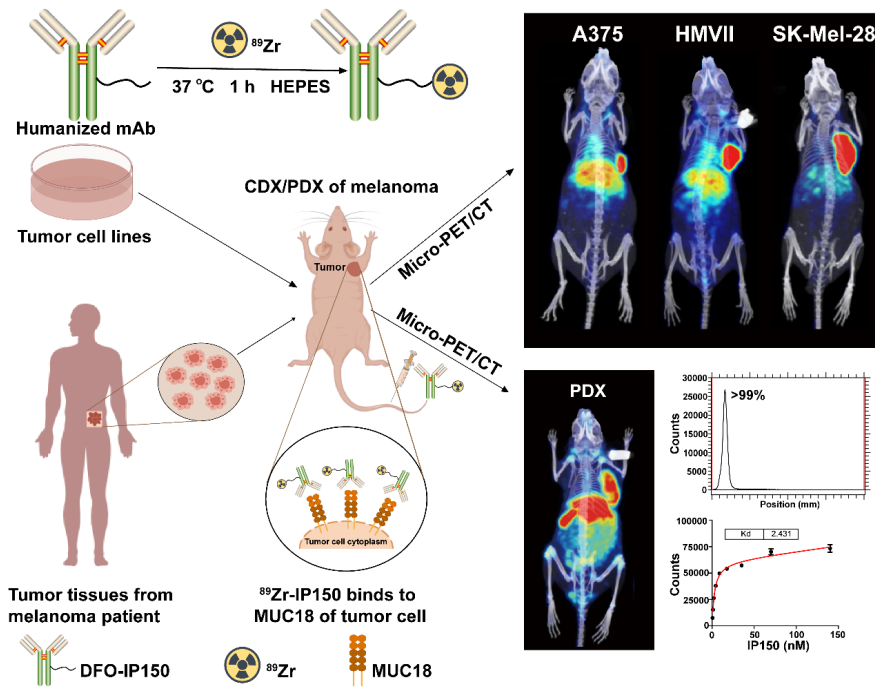
\*Zhi Yang. Tel: 86+88196196, E-mail: [pekyz@163.com](mailto:pekyz@163.com).

\*Hua Zhu. Tel: 86+88196495, E-mail: [zhuhuananjing@163.com](mailto:zhuhuananjing@163.com).

**Running title:** MUC18-targeted humanized monoclonal antibody immune-PET imaging

**Acknowledgments:** Not applicable.

### Graphical Abstract



$^{89}\text{Zr}$ -IP150 can be used to image various CDXs of humanized melanoma, and for the first time, the clinical conversion potential of  $^{89}\text{Zr}$ -IP150 was explored using a more clinically representative melanoma PDX model.

### MUC18-targeted humanized monoclonal antibody immunePET imaging and patient-derived tumor xenograft visualization

#### Abstract

**Background:** In the context of precision diagnosis for various subtypes of melanoma, identifying biomarkers with clinical translational potential from a molecular standpoint is crucial for a more comprehensive characterization of the disease. MUC18 is highly expressed in both tumor cells and tumor vasculature in major melanoma subtypes and is restricted to normal tissues.

**Methods:** A noninvasive imaging approach for MUC18 in melanoma utilizing an immune Positron Emission Tomography (PET) radionuclide-conjugated drug (RDC) with an  $^{89}\text{Zr}$ -labeled humanized anti-MUC18 monoclonal antibody (mAb) was developed. A375, Sk-Mel-28, HMVII, and A549 cells and tumor model mice were conducted. Immuno-PET was employed to assess the specificity and targeting of three distinct

melanoma cell line-derived xenografts (CDXs) and patient-derived tumor xenografts (PDXs) in immunodeficient mice.

**Results:** The developed RDC, named  $^{89}\text{Zr}$ -IP150, demonstrated robust in vitro stability and high binding affinity, ensuring reliable and specific PET imaging of small, medium, and large subcutaneous tumors in human melanoma mouse xenotransplantation models. Notably, for the first time, the clinical translational potential of  $^{89}\text{Zr}$ -IP150 was successfully validated using a PDX model.

**Conclusions:** These findings present a noninvasive, real-time method for the early screening of MUC18 (+) melanoma patients and are important for studying the early-stage biological distribution of MUC18-targeted antibody-drug conjugates (ADCs).

**Keywords:** Immuno-PET imaging; Humanized mAb; Melanoma; PDX model

## Introduction:

Melanoma stands out as the most lethal form of skin cancer and originates from the malignant transformation of melanocytes<sup>[1]</sup>. These melanocytes, which arise from the neuroectoderm, migrate extensively throughout the body, including through the skin, uvea, mucous membranes, inner ear, and rectum. These cells are highly dendritic cells that produce melanin to shield against light damage<sup>[2]</sup>. According to statistics, an estimated 100,640 individuals will receive a new diagnosis of this invasive disease, and 8,290 individuals will die from melanoma of the skin in America by 2024<sup>[3]</sup>. Benefiting from advancements in early clinical detection and systemic treatment, the 5-year relative survival rate for skin melanoma patients increased to 93% between 2011 and 2017, a notable improvement from 82% in the mid-1970s<sup>[4]</sup>. Approximately 71% of melanoma patients receive a diagnosis at stage 1, with a remarkable 5-year relative survival rate nearing 100%. In addition, although the incidence of mucosal melanoma is low, due to the lack of early identification, its mortality rate is much greater than that of skin melanoma patients. Consequently, the early screening and detection of melanoma holds profound significance in guiding subsequent treatment choices and enhancing overall survival rates.

MUC18, also known as melanoma cell adhesion molecule (MCAM), is a transmembrane glycoprotein identified by Johnson et al. using the anti-human melanoma monoclonal antibody MUC18, which exhibits distinct expression differences between malignant melanoma cells and normal cells<sup>[5]</sup>. The resulting amino acid sequences revealed that MUC18 belongs to the immunoglobulin superfamily and shares significant similarity with the sequences of a group of nerve cell adhesion molecules expressed during organogenesis<sup>[6, 7]</sup>. As research progressed, MUC18 acquired various names, including CD146, melanoma adhesion molecule, melanoma-associated antigen A32, melanoma-associated antigen Mel-CAM, MET-CAM, and HEMCAM. Through bidirectional interactions with multiple specific ligands, such as laminin 411 and 421, galectin-1 and -3, S100A8/A9, and matriptase, MUC18 actively participates in numerous physiological and pathological cellular processes. Overexpression of MUC18 is commonly observed in most malignancies and is implicated in nearly every stage of cancer development and progression, particularly in vascular and lymphatic metastasis<sup>[8]</sup>. In recent decades, immunotherapy, including immune checkpoint blockade, has revolutionized cancer treatment<sup>[9, 10]</sup>. However, T-cell exhaustion is associated with decreased efficacy of immune checkpoint inhibitors and adoptive T-cell therapies<sup>[11]</sup>, and a significant number of patients still do not benefit from current forms of immunotherapy. Given the unusually high expression of MUC18 in a variety of tumors and its various roles in reshaping the tumor microenvironment, specific diagnosis and targeted therapies targeting MUC18 may overcome this barrier<sup>[12]</sup>.

Routine clinical methods, such as immunohistochemistry (IHC) and fluorescence in situ hybridization (FISH), for analyzing biomarker expression levels in tumors are invasive and lack real-time access to biomarker expression throughout the body. Recent advancements in nuclear medicine devices, such as whole-body positron emission tomography/computed tomography (PET/CT), now enable the acquisition of higher quality images while reducing patient and staff doses and acquisition times<sup>[13-15]</sup>.

Imaging targeting MUC18 currently relies predominantly on PET probes, with radiolabeled precursors en-

compassing MUC18-targeted monoclonal antibodies (mAbs), F(ab')<sub>2</sub> fragments, and scFv<sup>[16]</sup>. To align with the precursors' half-life, nuclides such as <sup>52</sup>Mn, <sup>64</sup>Cu, <sup>68</sup>Ga, <sup>89</sup>Zr, and <sup>99m</sup>Tc are utilized for labeling. These probes have been investigated in various cancer models, including models of malignant melanoma<sup>[17, 18]</sup>, brain tumors<sup>[19, 20]</sup>, lung cancer<sup>[21, 22]</sup>, hepatocellular carcinoma<sup>[23]</sup>, and breast cancer<sup>[24, 25]</sup>. Despite the significance of these studies, the antibodies YY146 and Fab'2 TsCD146 employed in the present study are nonhumanized antibodies. In clinical applications, the human body recognizes these monoclonal antibodies as alloproteins, leading to immune rejection and faster clearance rates. Consequently, there is a compelling need to develop humanized mAb-based radiopharmaceuticals targeting MUC18 to address these challenges. We previously employed a Zr-89-labeled humanized antibody for CLDN18.2-targeted imaging<sup>[26]</sup>.

Here, we developed an MUC18-specific probe through the radiolabeling of <sup>89</sup>Zr with a humanized monoclonal antibody, IP150. The resulting radiolabeled probe, denoted RDC (<sup>89</sup>Zr-IP150), demonstrated robust binding specificity for MUC18 *in vitro* and exhibited reliable imaging capabilities for both skin and mucosal CDX models *in vivo*. To enhance the clinical relevance of this study, probe specificity was also assessed in melanoma PDX models. These findings offer a promising approach for the early diagnosis of melanoma patients, signifying the importance of exploring the biological distribution of ADCs and guiding therapy.

## Materials and Methods

General: <sup>89</sup>Zr is produced using a medical cyclotron via the nuclear reaction of <sup>89</sup>Y (p, n)<sup>89</sup>Zr (Peking University Cancer Hospital & Institute). MUC18 mAb (IP150, a humanized antibody) was generated in a CHO expression system and purified by MabSelect<sup>TM</sup> Sure Resin (GE Healthcare Life Sciences).

### 2.1 Cell culture and animal models

The human melanoma cell lines A375, SK-Mel-28, and HMVII and the human non-small cell lung cancer cell line A549 were obtained from Procell Life Science & Technology Co., Ltd.; A375, SK-Mel-28, and A549 were cultured in standard Dulbecco's modified Eagle's medium or RPMI-1640 (Bioskan) supplemented with penicillin (Bioskan), streptomycin (Invitrogen), and FBS (Sigma-Aldrich) at 37 °C in a 5% CO<sub>2</sub> atmosphere; and HMVII was cultured in Ham's F-10 Nutrient Mixture (Giboco) supplemented with 10% FBS [Sigma-Aldrich] at 37 degC with 5% CO<sub>2</sub>. When the cells reached ~ 80% confluence, they were used for *in vitro* and *in vivo* experiments.

A375 and HMVII tumor xenografts were induced in 4- to 5-week-old female athymic nude mice (Beijing Vital River Laboratory Animal Technology Co., Ltd.) via the injection of 1 x 10<sup>6</sup> cells (suspended in 100 μL of PBS) into the underarm. For the SK-Mel-28 and A549 cell models, cells were suspended in 100 μL of a 1:1 mixture of PBS and Matrigel (BD Biosciences), and the animals were used for *in vivo* experiments 3 weeks after implantation when the tumors reached in diameter. Human melanoma PDX models were generated by Department of Renal Melanoma, Peking University. All animal experiments were completed in accordance with the relevant guidelines and regulations of Beijing Cancer Hospital.

### 2.2 Differential expression and prognosis of MUC18 in GEPIA2

The internet database GEPIA2 (Gene Expression Profiling Interactive Analysis 2) was used to assess MUC18 gene expression in several types of tumors and normal tissues by matching TCGA normal and GTEx data. Survival maps, survival curves for overall survival (OS) and disease-free survival (DFS) were generated based on the gene expression patterns of 33 different cancers using GEPIA2 through log-rank and Mantel-Cox tests, and the group cutoff was based on the median (cutoff-high: 50%, cutoff-low: 50%). The hazard ratio (HR) was calculated based on the Cox PH model, and the confidence interval (CI) was 95%. Special survival graphs with log-rank p values were generated using the "Survival Analysis" module in GEPIA2. The results were considered to be statistically significant if  $p < 0.05$ . The data were downloaded from <http://gepia2.cancer-pku.cn/#analysis>.

### 2.3 DFO conjugation and <sup>89</sup>Zr-labeling of IP150

The MUC18-specific mAb IP150 was conjugated to DFO-NCS (Innochem) via lysine residues. DFO was

prepared at 10 mg/mL (20  $\mu$ L) in neat DMSO and mixed with 0.1 M  $\text{Na}_2\text{CO}_3$  (pH 9.0, 200  $\mu$ L). Then, 500  $\mu$ g of mAb was added and incubated at 37  $^\circ\text{C}$  for 60 min. The nonconjugated chelate was removed by size exclusion chromatography using metal-free PBS as the eluent and a PD-10 column (Cytiva). The products were collected into five centrifuge tubes (500  $\mu$ L). Then, the concentration was determined by a NanoDrop, and the average molecular weight of the mAb (20  $\mu$ L) before and after the reaction was analyzed by matrix-assisted laser desorption/ionization time-of-flight mass spectrometry (MALDI-TOF-MS).

The  $^{89}\text{Zr}$ -IP150 probe was labeled by reacting  $^{89}\text{Zr}$ -oxalate and DFO-IP150 at 37 for 60 min (Figure 1A), and  $^{89}\text{Zr}$ -oxalate (48.1 MBq; 125  $\mu$ L in 1 M oxalic acid) was mixed with HEPES buffer (1375  $\mu$ L, pH 7.0). Then, 200  $\mu$ L of DFO-IP150 (200  $\mu$ g) was added to the mixed liquor. After incubating at room temperature for 60 minutes, the reaction mixture was purified on a PD-10 column using metal-free PBS as the eluent. Similar to DFO conjugation,  $^{89}\text{Zr}$ -IP150 was collected in five centrifuge tubes (500  $\mu$ L). Before and after purification, 3  $\mu$ L of sample was spotted on a TLC silica gel strip and developed in 0.05 M citric acid (pH 5.0)/saturated EDTA as the eluent, after which the radiolabeling rate and radiochemical purity were analyzed by BIOSCAN. Two hundred microliters of  $^{89}\text{Zr}$ -IP150 in 5% HSA (Baxter) was incubated at 4 to assess the in vitro stability by analyzing the radiochemical purity every 24 h.

#### 2.4 Binding properties of IP150 and DFO-IP150 to the

##### *MUC18 protein*

Enzyme-linked immunosorbent assay (ELISA) is one of the most specific and straightforward assays for detecting biomolecules in research and clinics. ELISA was used to analyze whether the ability of the mAb to bind to the MUC18 target changed before and after DFO conjugation. First, the MUC18 protein (Sino Biological) was diluted to 1  $\mu$ g/mL with coating solution (0.1 M carbonate buffer, pH 9.5) and then plated on a 96-microtiter plate well (100  $\mu$ L/well) with a pipette at 4  $^\circ\text{C}$  overnight. After the 96-well plates were washed with PBST 5 times, nonspecific sites were blocked with 5% skim milk powder (200  $\mu$ L/well, 37  $^\circ\text{C}$ , 2 h), and the plates were subsequently discarded and washed with PBST 5 times. The concentrations of the primary antibodies IP150 and DFO-IP150 were diluted to 0.000032-9.9  $\mu$ g/mL, and then 100  $\mu$ L was added to each well (n=4, 37  $^\circ\text{C}$ , 2 h). Then, the cells were incubated with a rabbit anti-human secondary antibody (1:3000, 100  $\mu$ L/well, 37  $^\circ\text{C}$ , 2 h). After incubation with TMB (100  $\mu$ L/well, Solarbio) in the dark for 3-5 minutes, 12.5%  $\text{H}_2\text{SO}_4$  (50  $\mu$ L/well) was added to terminate the color development, and the OD450 nm was read with an enzyme marker.

#### 2.5 Micro-PET/CT Imaging in Melanoma Tumor Xenografts

Xenograft tumor models (CDX/PDX) were used to noninvasively evaluate the specificity and targeting of the  $^{89}\text{Zr}$ -labeled antibody against MUC18 in vivo. Experiments were performed when the tumors reached 5–15 mm in diameter. Images of models injected with 3.7 MBq  $^{89}\text{Zr}$ -IP150 (200  $\mu$ L, 100  $\mu$ Ci) via the tail vein were collected at specific time points (4, 24, 48, 72, 96, 120 and 168 h, p.i.). One milligram of IP150 was injected intravenously in the blocked group in advance.

The PET collection time was 900 s, and CT images were acquired after PET collection and reconstruction. Images were processed using VivoQuant postprocessing software. PET imaging raw data were converted into false-colored maximum intensity projections on a color scale expressed as SUVs, and quantitative results were obtained by mapping regions of interest (ROIs).

#### 2.6 $^{18}\text{F}$ -Fluorodeoxyglucose ( $^{18}\text{F}$ -FDG) PET Imaging

Before  $^{18}\text{F}$ -FDG PET imaging, the mice must be kept fasting for at least 8 hours. Each anesthetized mouse was injected with 7.4 MBq  $^{18}\text{F}$ -FDG (200  $\mu$ L, 200  $\mu$ Ci) through the tail vein and kept under anesthesia until imaging (60 min, p.i.). The PET collection time was 900 s, and quantitative results were obtained by mapping the ROI on the tumor region.

#### 2.7 Statistical analysis

The results are presented as the means  $\pm$  SDs and were plotted using GraphPad Prism software. Comparisons between two groups were analyzed by unpaired, two-tailed  $t$  tests. Differences were considered statistically significant if  $p < 0.05$ .

## Results

### 3.1 MUC18 serves as a Crucial Biomarker for Tumors

The expression difference of MUC18 between tumor and normal tissues was evaluated by pairing TCGA and GTEx data. MUC18 was upregulated in 8 cancers—head and neck squamous cell carcinoma (HNSC), kidney renal clear cell carcinoma (KIRC), lymphoid neoplasm diffuses large B-cell lymphoma (DLBC), cholangiocarcinoma (CHOL), glioblastoma multiforme (GBM), liver hepatocellular carcinoma (LIHC), pancreatic adenocarcinoma (PAAD), and thymoma (THYM)—compared with normal tissues (Figure 1A). Analysis of the pancancer cohort from the GEPIA2 database revealed that patients with high MUC18 expression in the Mesothelioma (MESO, HR=2.8), GBM (HR=1.5), Brain Lower Grade Glioma (LGG, HR=2.2), and Cervical squamous cell carcinoma and endocervical adenocarcinoma (CESC, HR=1.6) cohorts had significantly reduced OS, and patients with high MUC18 expression in the Adrenocortical carcinoma (ACC, HR=2.8), Kidney Chromophobe (KICH, HR=12), LGG (HR=1.5), and Uveal Melanoma (UVM, HR=3.2) cohorts had significantly reduced DFS, suggesting that high MUC18 expression adversely affects the prognosis of patients with these tumors (Figure 1B).

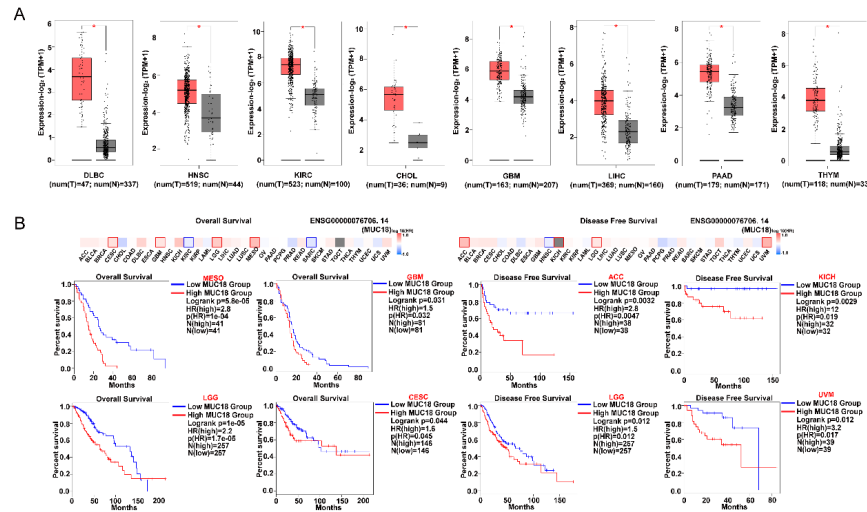


**Figure 1.** Analysis of GEPIA2 outputs. (A) Comparisons of MUC18 expression levels between tumor and nontumor control tissues (the expression levels were significantly different between tumor and normal tissues); red, tumor expression levels; black, nontumor expression levels; \*,  $p < 0.05$ . (B) The prognostic impact of MUC18 expression based on the survival heatmap. The heatmap shows the hazard ratios on a logarithmic scale ( $\log_{10}$ ) on MUC18. The red and blue blocks denote higher and lower risks, respectively. The rectangles with red frames mean the significant unfavorable results in prognostic analyses.

### 3.2 Production and Characterization of $^{89}\text{Zr}$ -IP150

The MALDI-TOF-MS results showed that the molecular weight of the IP150 mAb was 148533.772 D (Figure 2B), the molecular weight of the DFO-IP150 mAb was 151917.775 D (Figure 2C), and about ~four DFO were conjugated to each IP150 molecule. The EC<sub>50</sub> values of the MUC18 protein for IP150 and DFO-IP150 were 2.2 nM ( $R^2=0.87$ ) and 3.07 nM ( $R^2=0.96$ ), respectively (Figure 2E), suggesting that the conjugation of DFO has no impact on the binding activity of IP150. After 60 minutes of reaction at 37 °C, the radiolabeling rate was 97.5% (Figure 2D), and the radiochemical purity was determined with a TLC silica gel strip.  $^{89}\text{Zr}$ -IP150

has a high radiochemical yield ( $\sim 99\%$ ) and high specific activity ( $28.22 \pm 8.53$  GBq/ $\mu\text{mol}$ ) (Supplementary Figure 1A and Table 1). The  $^{89}\text{Zr}$  loss of the  $^{89}\text{Zr}$ -IP150 probe was less than 5% after 120 hours (incubation in PBS and 5% HSA at 37 °C), indicating that the probe has good stability in vitro (Supplementary Figure 1B, 1C), which is acceptable for preclinical studies.

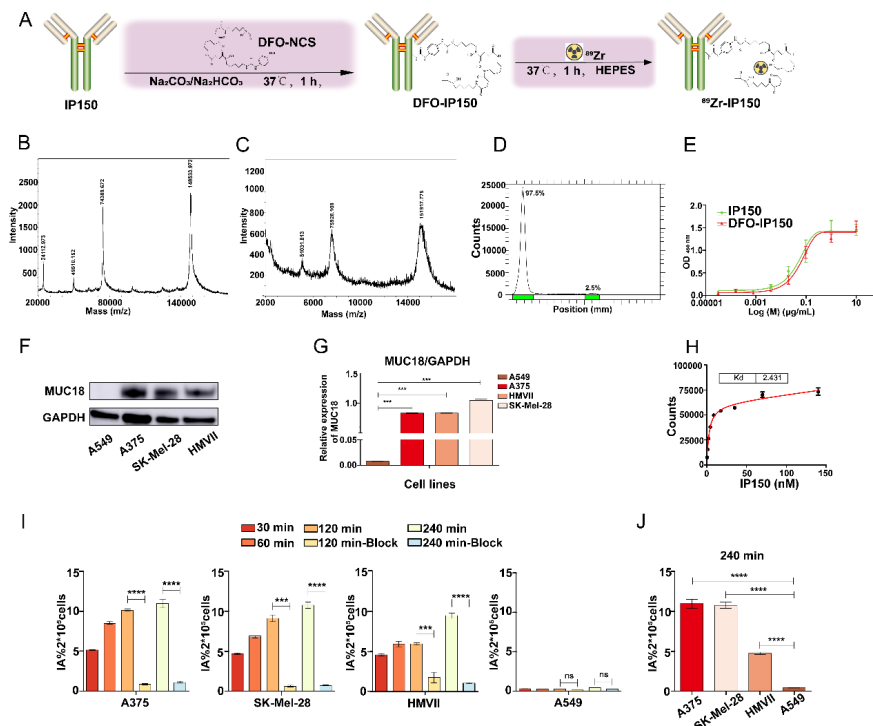


**Figure 2.** (A) Scheme of  $^{89}\text{Zr}$ -labeled IP150. (B), (C) Average molecular weights of IP150 and DFO-IP150. (D) The radiochemical purity of unpurified  $^{89}\text{Zr}$ -IP150. (E) The binding ability of IP150 and DFO-IP150 to the MUC18 protein. (F) (G) Protein expression levels of MUC18 in different cancer cell lines. (H) Receptor binding assay of  $^{89}\text{Zr}$ -IP150 in the A375 cell line. (I) Cellular uptake of  $^{89}\text{Zr}$ -IP150 in A375, SK-Mel-28 (cutaneous melanoma), and HMVII (mucosal melanoma) cells. (J) Comparison of the uptake in four cell lines at 240 min. \*\*\*,  $p < 0.001$ ; \*\*\*\*,  $p < 0.0001$ .

Parameters	Quality Control Specification	Quality Control Result
Appearance	Clear, colorless	Clear, colorless
Volume	1-2 mL	1.5 mL
pH	5.0-8.0	7.4
Radiochemistry purity (iTLC)	> 95%	>99%
Ethanol	<5%	Pass
Endotoxins	< 15 EU/mL	Pass
Sterility	Sterile	Pass
Specific activity (GBq/ $\mu\text{mol}$ )	18.5 - 296.0 GBq/ $\mu\text{mol}$	$28.22 \pm 8.53$

### 3.3 MUC18 Expression in Each Cell Model

The MUC18 protein was positively expressed in the melanoma cell lines A375, HMVII and SK-Mel-28 but was not expressed in the A549 cell line (Figure 2F). The results showed that the expression of MUC18 was

highest in SK-Mel-28 cells ( $1.04 \pm 0.04$ ), similar in A375 cells and HMVII cells ( $0.83 \pm 0.01$ ,  $0.83 \pm 0.02$ ), and lowest in A549 cells ( $0.01 \pm 0.001$ ) (Figure 2G). These findings suggested that the three melanoma cell lines can be used as positive models and that the A549 cell line can be used as a negative model.

### 3.4 $^{89}\text{Zr}$ -IP150 cell uptake and affinity test

The in vitro binding assay of  $^{89}\text{Zr}$ -P150 to the MUC18 (+) cell line A375 demonstrated a  $K_d$  of 2.431 nM and an  $R^2$  of 0.9718 (Figure 2H).

The time-dependent uptake of  $^{89}\text{Zr}$ -IP150, which could be blocked by the unconjugated IP150 mAb, was observed in MUC18 (+) A375, SK-Mel-28 and HMVII cells, but no uptake of  $^{89}\text{Zr}$ -IP150 was observed in MUC18 (-) A549 cells (Figure 2I). At 240 min, the cell uptake was  $10.96 \pm 1.11$  vs.  $1.13 \pm 0.22$  IA%/2 $\times 10^5$  cells in A375,  $10.76 \pm 0.77$  vs.  $0.75 \pm 0.11$  in the IA%/2 $\times 10^5$  SK-Mel-28 cells,  $9.49 \pm 0.66$  vs.  $1.05 \pm 0.15$  in the IA%/2 $\times 10^5$  HMVII cells, respectively ( $p < 0.001$ ). Moreover, at 240 min (Figure 2J), the uptake of  $^{89}\text{Zr}$ -IP150 by MUC18 (-) A549 cells ( $0.43 \pm 0.05$  IA/2 $\times 10^5$  cells) was significantly lower than that by the three MUC18 (+) cell lines ( $p < 0.001$ ).

### 3.5 Metabolism of $^{89}\text{Zr}$ -IP150 in KM Mice and Radiation Dose Estimation

As shown in Supplementary Figure 1D-F, the micro-PET/CT imaging results showed that  $^{89}\text{Zr}$ -IP150 was metabolized by the liver in KM mice from 2 to 120 hours post injection. The signal of  $^{89}\text{Zr}$ -IP150 was clearly visible in the blood pool at 2 hours, the SUVmax was  $0.90 \pm 0.09$  and then gradually decreased, and the SUVmax was only  $0.44 \pm 0.02$  at 120 hours. In addition,  $^{89}\text{Zr}$ -IP150 also had high uptake in the spleen, but the uptake decreased gradually from 2 to 120 hours ( $0.80 \pm 0.05$  to  $0.48 \pm 0.03$ ). The uptake of  $^{89}\text{Zr}$ -IP150 in other normal organs (lungs, muscle, bone, and brain) was minimal.

Then, the human organ radiation dosimetry estimation of  $^{89}\text{Zr}$ -IP150 in adult female patients was calculated. As shown in Table 2, the organ predicted to have the highest absorbed dose in humans was the liver (0.218 mGy/MBq), followed by the spleen (0.211 mGy/MBq) and lung (0.195 mGy/MBq). The effective dose was 0.065 mSv/MBq, indicating that when a person injected 37 MBq  $^{89}\text{Zr}$ -IP150, the radiation dose received was 2.41 mSv, which is acceptable for routine nuclear medicine research.

**Table 2.** Human Organ Radiation Dosimetry Estimation of  $^{89}\text{Zr}$ -IP150 in Adult Female Patients Using OLINDA/EXM 1.0

Target Organ	Total (mGy/MBq)
Adrenals	1.10E-01
Brain	6.99E-02
Breasts	2.25E-02
Esophagus	7.22E-02
Eyes	1.69E-02
Gallbladder Wall	6.38E-02
Left colon	3.48E-02
Small Intestine	1.23E-01
Stomach Wall	5.47E-02
Right colon	3.22E-02
Rectum	6.37E-02
Heart Wall	1.08E-01
Kidneys	1.17E-01
Liver	2.18E-01
Lungs	1.95E-01
Ovaries	1.73E-02
Pancreas	6.73E-02
Salivary Glands	1.66E-02
Red Marrow	3.14E-02

Osteogenic Cells	3.71E-02
Spleen	2.11E-01
Thymus	6.37E-02
Thyroid	3.19E-02
Urinary Bladder Wall	1.25E-02
Uterus	2.48E-02
Total Body	3.02E-02
Effective Dose(mSV/MBq)	6.45E-02

### 3.6 Evaluation of IP150-based radio-conjugates in the CDX/PDX melanoma model

Four in vivo CDX tumor models were established to validate the ability of  $^{89}\text{Zr}$ -IP150 to target MUC18 by imaging. IHC staining confirmed that the A375, HMVII and SK-Mel-28 CDXs were MUC18 (+), while the A549 CDX was MUC18 (-) (Figure 3B). Moreover,  $^{89}\text{Zr}$ -IP150 had a high PET signal in the MUC18(+) A375, HMVII, and SK-Mel-28 tumors and a low signal in the MUC18(-) A549 tumor (Figure 3A). In the A375 model (small tumor), the time-dependent accumulation of  $^{89}\text{Zr}$ -IP150 in the tumor was visualized by static PET/CT at 2, 24, 48, 72, 96, 120, and 168 hours p.i. The tumor was visible at 24 hours p.i., and a high contrast image (tumor/background) was available at 48 p.i.; nearly no radiotracer was detected in normal tissues except the liver, and no significant residue or accumulation of the  $^{89}\text{Zr}$  conjugate was detected in the joints. According to image semiquantitative uptake calculations, the tumor-specific signal increased mainly from 2 to 24 h p.i., with an SUVmax ranging from  $0.69\pm 0.03$  to  $2.56\pm 0.12$ , and the tumor uptake continued to increase to  $5.67\pm 0.29$  at 168 p.i. (Supplementary Figure 2A). Furthermore, the specificity of  $^{89}\text{Zr}$ -IP150 to MUC18 binding was confirmed by intravenous preinjection (24 hours before injection of  $^{89}\text{Zr}$ -IP150) with 1 mg of unlabeled IP150 mAb (Figure 4A). The SUVmax of the tumor at 2 hours was  $0.72\pm 0.05$ , which was not significantly different from that of the nonblock group ( $p = 0.54$ ), but the accumulation of the tracer at the tumor (Supplementary Figure 2A and 2B) was significantly different ( $p < 0.05$ ) at 24 hours ( $2.56\pm 0.12$  vs.  $0.39\pm 0.02$ ,  $3.16\pm 0.12$  vs.  $1.68\pm 0.14$ ,  $4.22\pm 0.14$  vs.  $1.84\pm 0.13$ ,  $4.38\pm 0.10$  vs.  $1.83\pm 0.05$ ,  $4.87\pm 0.14$  vs.  $1.87\pm 0.13$ , and  $5.57\pm 0.29$  vs.  $1.95\pm 0.08$ ). In the HMVII model (medium tumor),  $^{89}\text{Zr}$ -IP150 also showed visible tumor uptake at 24, 48, 72 and 120 hours and peaked uptake at 96 hours, with an SUVmax of  $7.11\pm 0.08$  (Supplementary Figure 2C and 2D). Similarly, tumor uptake was also significantly decreased ( $p < 0.05$ ) in the block group at 24 hours ( $2.99\pm 0.02$  vs.  $0.96\pm 0.06$ ,  $4.99\pm 0.12$  vs.  $0.09\pm 0.04$ ,  $5.44\pm 0.09$  vs.  $1.32\pm 0.02$ ,  $7.11\pm 0.08$  vs.  $1.34\pm 0.06$ ,  $3.69\pm 0.04$  vs.  $1.49\pm 0.05$ , and  $3.63\pm 0.06$  vs.  $1.52\pm 0.09$ ). Moreover,  $^{89}\text{Zr}$ -IP150 was also a good indicator of the location of SK-Mel-28 (large tumor) (Supplementary Figure 2E). For the A549 model (MUC18-), almost no radioactive uptake was observed at the tumor site, with a low SUVmax of  $0.72\pm 0.04$  (Figure 3A and 4A).

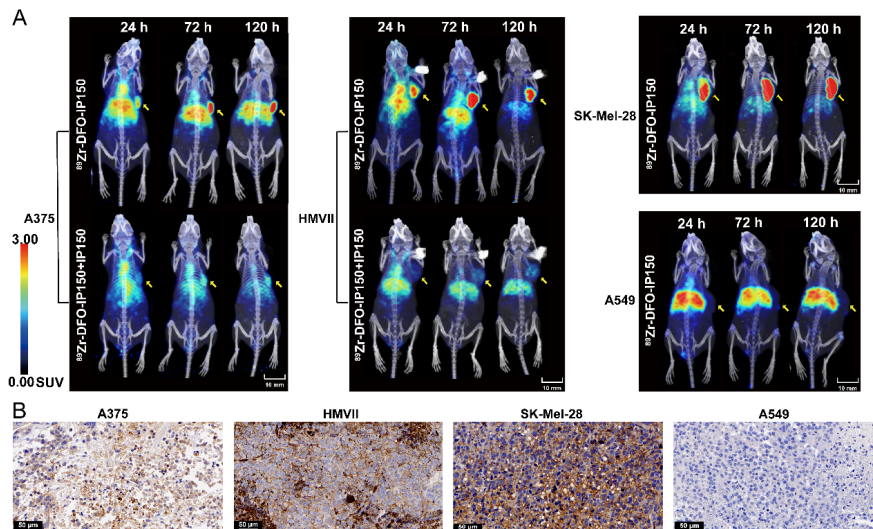


**Figure 3 . (A)** Micro-PET/CT images of A375 tumor-bearing mice after administration of  $^{89}\text{Zr}$ -IP150 ( $n = 3/\text{group}$ ). **(B)** IHC staining of MUC18 in tumors. Scale bar = 50  $\mu\text{m}$ .

Further analysis revealed that the tumor uptake of  $^{89}\text{Zr}$ -IP150 at 24 h ( $R^2 = 0.9543, p = 0.0231$ ), 72 h ( $R^2 = 0.9379, p = 0.0316$ ), and the peak timepoint ( $R^2 = 0.9460, p = 0.0274$ ) correlated with the expression levels of MUC18 in A375, HMVII, SK-Mel-28, and A549 cells (Figure 4C).

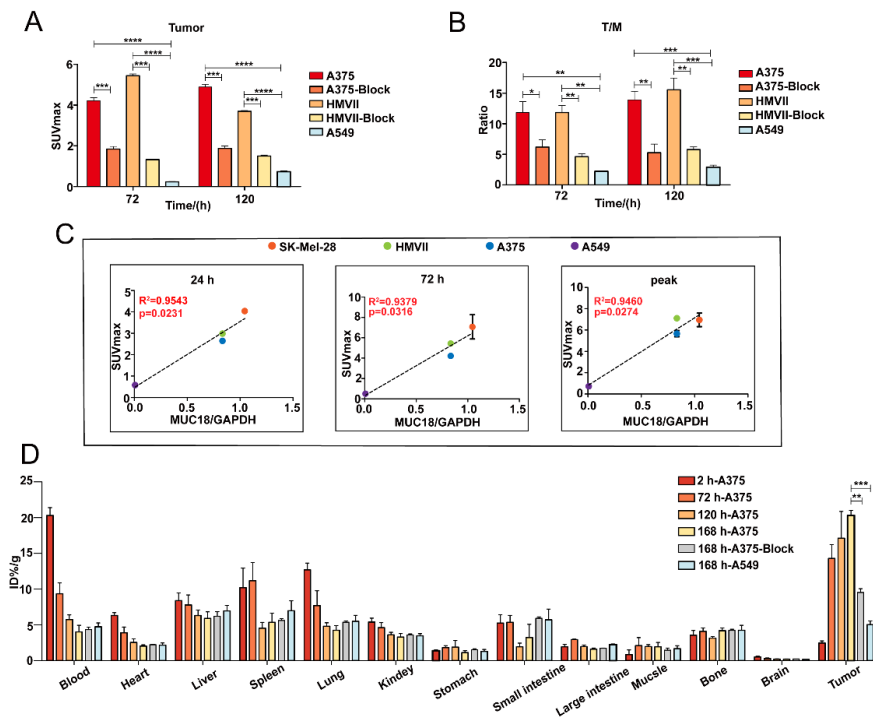


**Figure 4. (A) (B)** Region of interest (ROI) analysis of the PET images. The values are presented as the SUVmax ( $n = 3$ ). **(C)** Correlation analysis between the SUVmax and CD146 expression. **(D)** Ex vivo

biodistributions of the A375 and A549 cell models ( $n = 3/\text{group}$ ). \*,  $p < 0.05$ ; \*\*,  $p < 0.01$ ; \*\*\*,  $p < 0.001$ ; \*\*\*\*,  $p < 0.0001$ .

To further evaluate the specific imaging ability of  $^{89}\text{Zr}$ -IP150 for melanoma,  $^{18}\text{F}$ -FDG, the most commonly used PET imaging tracer in the clinic, was used as a control. No significant difference in radioactive concentration was detected between the A375 and HMVII tumors at 1 h p.i., and  $^{18}\text{F}$ -FDG accumulated mainly in metabolic organs such as the heart and kidneys (Figure 5A). The uptake of  $^{18}\text{F}$ -FDG in tumors was significantly lower than that of  $^{89}\text{Zr}$ -IP150 in both the A375 ( $0.96 \pm 0.06$  vs.  $5.57 \pm 0.29$ ) and HMVII ( $1.28 \pm 0.03$  vs.  $7.11 \pm 0.08$ ) models ( $p < 0.001$ ) (Figure 5B). In addition, the tumor/muscle ratio of  $^{18}\text{F}$ -FDG was also significantly lower than that of  $^{89}\text{Zr}$ -IP150 ( $0.96 \pm 0.06$  vs.  $21.48 \pm 4.40$  in A375 and  $2.12 \pm 0.06$  vs.  $21.33 \pm 3.45$  in HMVII) (Figure 5C) ( $p < 0.0001$ ).

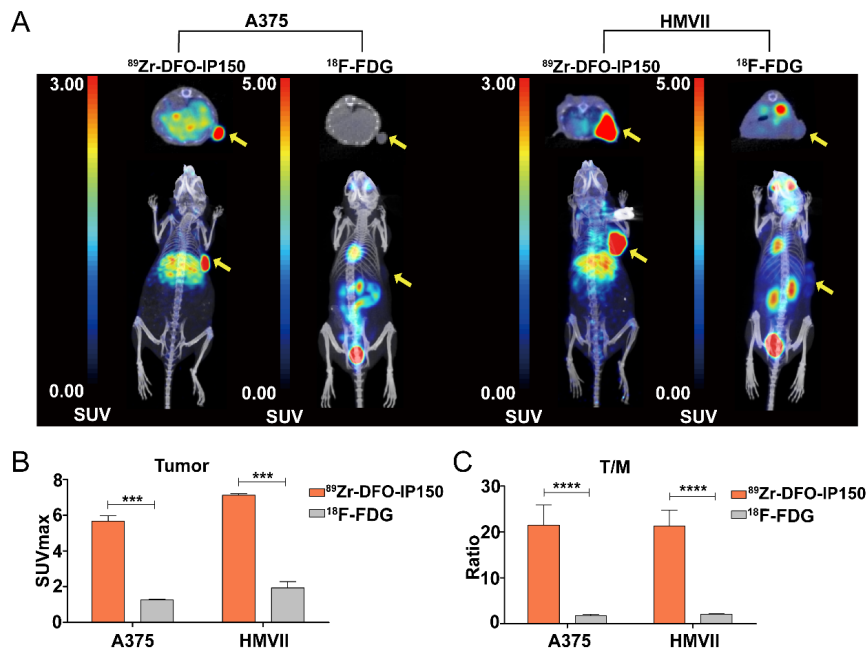


**Figure 5 . (A)** Comparison of the micro-PET/CT images of A375 and HMVII tumor-bearing mice after administration of  $^{89}\text{Zr}$ -IP150 or  $^{18}\text{F}$ -FDG via tail vein injection ( $n = 3/\text{group}$ ). **(B)**, **(C)** ROI and tumor/muscle ratio analysis of the PET images. The values are presented as the SUVmax ( $n = 3$ ). \*\*\*,  $p < 0.001$ ; \*\*\*\*,  $p < 0.0001$ .

To expand the clinical relevance of this study,  $^{89}\text{Zr}$ -IP150 was evaluated in a MUC18 (+) melanoma PDX model (Figure 6C). Significant uptake in the tumor was observed from 24 hours to 96 hours in the MIP and coronal images (Figure 6A). The maximum tumor uptake was reached at 24 hours, with an SUVmax of  $2.77 \pm 0.16$ , while the concentration of radioactivity in the heart decreased dramatically from 2 to 24 hours ( $3.23 \pm 0.04$  to  $0.70 \pm 0.04$ ) (Figure 6B). In addition, pathological staining of the PDX model revealed no specific expression of MUC18 in normal tissues, such as the heart, liver, spleen, lung, kidney, stomach, small intestine, large intestine, muscle and brain (Supplementary Figure 3).

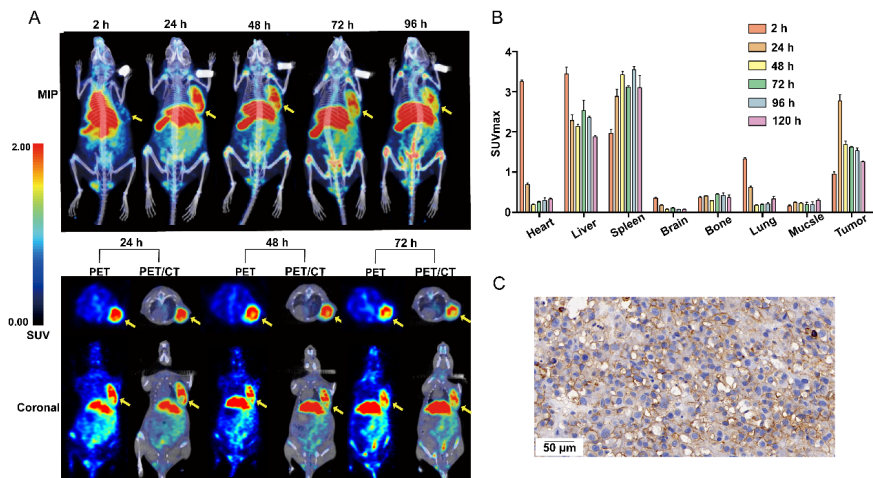


**Figure 6 . (A)** MIP images and coronal images of the human melanoma PDX model. **(B)** ROI analysis of the PET images; values are presented as the SUVmax (n = 3). **(C)** IHC staining of MUC18 in the PDX model.

### 3.7 Biodistribution in A375 and A549 tumor-bearing mice

As shown in Figure 4D, in the A375 xenograft model, the uptake values of  $^{89}\text{Zr}$ -IP150 in tumors at 72, 120, and 168 h were  $14.28 \pm 1.92$ ,  $17.13 \pm 3.74$ , and  $20.29 \pm 0.74$  ID%/g, respectively, which were greater than those in other normal tissues. Co-injection of the unlabeled precursor IP150 significantly reduced the tumor uptake of  $^{89}\text{Zr}$ -IP150 at 168 h p.i. by  $\sim 53\%$  ( $p < 0.01$ ) but had no impact on normal tissues. In addition, the uptake of  $^{89}\text{Zr}$ -IP150 in MUC18 (-) A549 tumors was comparable to that in normal tissues. These data suggest that the uptake of  $^{89}\text{Zr}$ -IP150 was indeed mediated by MUC18.

## Discussion

A growing body of research highlights the fundamental role of MUC18 in various pathologic processes; for example, MUC18 promotes atherosclerosis<sup>[27]</sup>, induces insulin resistance induced by obesity<sup>[28]</sup>, and contributes to the aggregation of infected red blood cells and lymphocytes<sup>[29]</sup>, and low expression of MUC18 also leads to insufficient blood flow in the interstitial vascular region<sup>[30]</sup>. The worldwide incidence of cutaneous melanoma has been increasing annually at a more rapid rate than that of any other type of cancer<sup>[31]</sup>. In contrast to the increasing incidence of skin melanoma, the incidence of mucosal melanoma has remained stable<sup>[32]</sup>. Early and accurate diagnosis of melanoma can greatly improve patient survival. In addition to the pathogenesis of each subtype of melanoma, the response to BRAF/MEK mutation-targeted small molecule and immune checkpoint therapy is different<sup>[17]</sup>; therefore, antibody-based drugs targeting overexpressed tumor-associated antigens, such as ADC, are a more universally effective treatment approach<sup>[33]</sup>. The dominant expression of MUC18 in melanomas (i.e., in approximately 70% of primary melanomas and 90% of lymph node metastases) makes this marker a potential candidate for identifying primary and metastatic melanomas; at present, the Class 1 biologic drug targeting MUC18 “ADC AMT-253 for injection”, which has been approved for clinical research in the treatment of advanced solid tumors. Moreover, we hypothesized that IP150 would serve as an ideal targeting vector for the delivery of RDC. Currently, there are reports of radionuclide probes targeting MUC18, but the antibodies used are mouse-anti-human mAbs<sup>[34]</sup>, which may cause a human anti-mouse antibody response and a low signal-to-noise ratio (SNR).

In this preclinical study, we propose an imaging approach that combines the high sensitivity and SNR of PET imaging with the biomolecular specificity of an anti-MUC18 humanized mAb for melanoma treatment.  $^{89}\text{Zr}$ -IP150 is created by a high labeling rate, superior radiochemical purity, and good stability. We used three different MUC18 (+) melanoma cell lines as well as a MUC18 (-) cell line to evaluate the specificity and targeting of the probe in vitro and separately constructed subcutaneous CDX xenograft tumor models

for *in vivo* studies. In A375, SK-Mel-28, and HMVII tumor-bearing mice,  $^{89}\text{Zr}$ -IP150 showed a favorable biodistribution in which it selectively accumulated in tumors, was quickly cleared from the blood, produced low background signals starting at 48 hours and persisted at 168 hours post injection at the tumor site with high sensitivity. Furthermore, the distribution of  $^{89}\text{Zr}$ -IP150 was desirable, with less accumulation in normal organs except for the liver, where exogenous antibodies are cleared<sup>[35]</sup>, which is desirable for PET imaging. Figure 2 and Figure 3 show that  $^{89}\text{Zr}$ -IP150 also has good specificity and targeting ability both *in vivo* and *in vitro* in a mucosal melanoma model (HMVII). Although the incidence of mucosal melanoma in the melanoma subtype is lower, the five-year survival rate is only 25% due to the lack of early and effective diagnosis, so our results may help these patients benefit from early and specific diagnosis to choose a better treatment plan. Because human melanomas consistently exhibit high glucose metabolism,  $^{18}\text{F}$ -FDG PET/CT imaging is particularly well suited for detecting these tumors<sup>[36]</sup>; however, we detected low radioactive signals of  $^{18}\text{F}$ -FDG in both the A375 and HMVII CDX models, possibly due to the inconsistency between human melanoma cell metabolism in immunodeficient mice and human melanoma metabolism.

$^{89}\text{Zr}$ -IP150 also showed significant uptake in MUC18 (+) PDX models of melanoma. We found that probe uptake in the PDX model continued for up to 96 hours. In addition, increased spleen uptake was also found in the PDX model.

These data may have implications for future clinical studies of ADC and CAR-T-cell administration or  $^{177}\text{Lu}/^{90}\text{Y}$ -labeled IP150 antibody-targeted therapy in patients. In addition, as an important tumor target, MUC18 is abnormally highly expressed in a variety of other tumors, and high expression of MUC18 leads to poor prognosis in a variety of tumors. In addition to these tumor types, studies have shown that reduced MUC18 expression plays a role in inhibiting tumorigenesis and carcinogenesis in colorectal cancer by inactivating the typical Wnt/ $\beta$ -catenin cascade<sup>[37]</sup>.

## Conclusions

In conclusion, this study introduced the preclinical application of a humanized radiolabeled MUC18-specific mAb probe, which was successfully employed to image various mouse models of humanized melanoma. Furthermore, the probe exhibited a promising targeting effect on tumors in a clinically representative melanoma PDX model. Importantly, the radiation dose in adults (0.065 mSv/MBq) was deemed relatively safe, supporting its potential for future clinical translation.

## Availability of data and materials

All data generated or analyzed during this study are included in this published article and its supplementary information files.

## Funding

This work was supported by the Youth Talent Support Program A002863, The National Natural Science Foundation (82171973, 82171980), and the Pilot Project (4th Round) to Reform Public Development of Beijing Municipal Medical Research Institute (2021-1).

## Author information

Qian Zhang, Haizhen Du, Xiuli Ma contributed equally to this work.

## Authors and Affiliations

Guizhou University Medicine College, Guizhou Province, Guiyang 550025, China

Qian Zhang, Zhi Yang, Hua Zhu

State Key Laboratory of Holistic Integrative Management of Gastrointestinal Cancers, Beijing Key Laboratory of Carcinogenesis and Translational Research, NMPA Key Laboratory for Research and Evaluation of Radiopharmaceuticals (National Medical Products Administration), Department of Nuclear Medicine, Peking University Cancer Hospital & Institute, No.52 Fucheng Rd, Beijing 100142, China

Qian Zhang, Song Liu, Xiangxing Kong, Muye Hu, Zhi Yang, Hua Zhu

Department of Renal Cancer and Melanoma, Key Laboratory of Carcinogenesis and Translational Research (Ministry of Education/Beijing), Peking University Cancer Hospital and Institute, No.52 Fucheng Rd, Beijing 100142, China

Haizhen Du, Qian Guo, Yan Kong, Jun Guo, Bin Lian

Multitude Therapeutics, 159 Tianzhou Road, Xuhui District, Shanghai 200030, China

Jing Shid, Yanfang Tangd, ShuHui Liud, Xun Meng

Department of Pathology, Peking University Cancer Hospital and Institute, Beijing, 100142, China

Xiuli Ma

### Author Contributions

Qian Zhang: Data curation, Formal analysis, Methodology, Writing – original draft. Haizhen Du, Xiuli Ma: Data curation, Formal analysis, Writing – original draf. Song Liu: Data curation. Formal analysis. Xiangxing Kong: Methodology. Muye Hu, Jing Shi, Yanfang Tang, ShuHui Liu, and Xun Meng: Software. Qian Guo, Yan Kong, Jun Guo: Supervision. Bin Lian: Conceptualization. Zhi Yang, Hua Zhu: Conceptualization, Resources.

All authors commented on previous versions of the manuscript. All the authors have read and approved the final manuscript.

### Ethics approval

All animal experiments were approved by the Institutional Animal Care and Use Committee of the Peking University Cancer Hospital & Institute.

### Conflicts of interest

The data generated in this study are available upon request from the 3 corresponding author. Intellectual properties protection has been filed by Multitude Therapeutics. No other potential conflict of interest relevant to this article was reported.

### Consent for publication

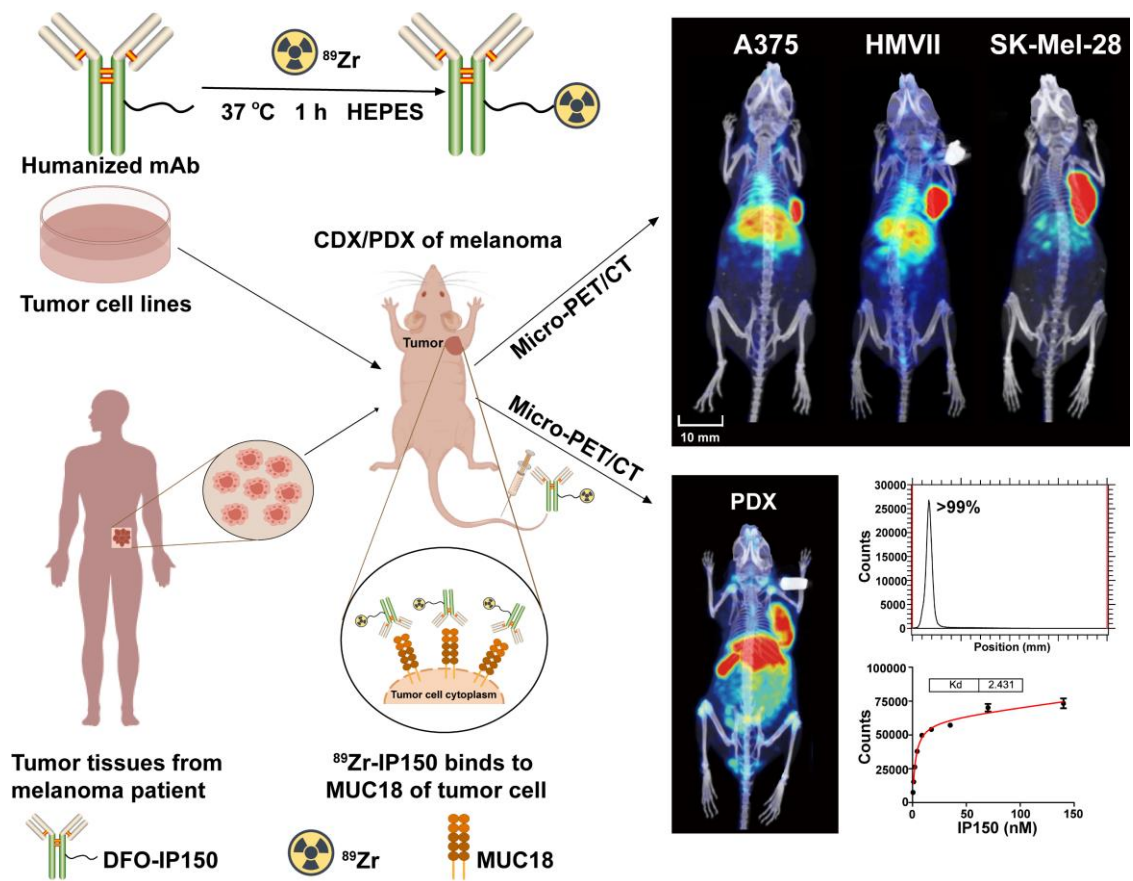
All authors are aware of and agree to the content of the paper and their being listed as a co-author of the paper.

All data generated or analyzed during this study are included in this published article [and its supplementary information files.

References[1] W. Guo, H. Wang, C. Li, *Signal Transduct Target Ther.* **2021** , *6* , 424.[2] J. A. Lo, D. E. Fisher,*Science.* **2014** , *346* , 945.[3] R. L. Siegel, A. N. Giaquinto, A. Jemal, *CA Cancer J Clin.* **2024** , *74* , 12.[4] H. G. Welch, S. Woloshin, L. M. Schwartz,*BMJ.* **2005** , *331* , 481.[5] J. M. Lehmann, B. Holzmann, E. W. Breitbart, P. Schmiegelow, G. Riethmuller, J. P. Johnson, *Cancer Res.* **1987** , *47* , 841.[6] J. M. Lehmann, G. Riethmuller, J. P. Johnson, *Proc Natl Acad Sci U S A.* **1989** , *86* , 9891.[7] M. Trzpis, P. M. McLaughlin, L. M. de Leij, M. C. Harmsen, *Am. J. Pathol.* **2007** , *171* , 386.[8] Z. Wang, X. Yan, *Cancer Lett.* **2013** , *330* , 150.[9] Y. Zhang, Z. Zhang, *Cell. Mol. Immunol.* **2020** , *17* , 807.[10] J. S. O'Donnell, M. Teng, M. J. Smyth, *Nat. Rev. Clin. Oncol.* **2019** , *16* , 151.[11] A. Chow, K. Perica, C. A. Klebanoff, J. D. Wolchok, *Nat. Rev. Clin. Oncol.* **2022** , *19* , 775.[12] Z. Wang, Q. Xu, N. Zhang, Du X, G. Xu, X. Yan, *Signal Transduct Target Ther.* **2020** , *5* , 148.[13] R. D. Badawi, H. Shi, P. Hu, S. Chen, T. Xu, P. M. Price, Y. Ding, B. A. Spencer, L. Nardo, W. Liu, J. Bao, T. Jones, H. Li, S. R. Cherry,*J. Nucl. Med.* **2019** , *60* , 299.[14] I. Alberts, J. N. Hunermund, G. Prenosil, C. Mingels, K. P. Bohn, M. Viscione, H. Sari, B. Vollnberg, K. Shi, A. Afshar-Oromieh, A. Rominger, *Eur J Nucl Med Mol Imaging.* **2021** , *48* , 2395.[15] R. Slart, C. Tsoumpas, A. Glaudemans, W. Noordzij, A. Willemsen, R. Borra, R. Dierckx, A. A. Lammertsma,

*Eur J Nucl Med Mol Imaging.* **2021** , *48* , 4236.[16] C. Li, L. Kang, K. Fan, C. A. Ferreira, K. V. Becker, N. Huo, H. Liu, Y. Yang, J. W. Engle, R. Wang, X. Xu, D. Jiang, W. Cai, *Bioconjug Chem.* **2021** , *32* , 1306.[17] W. Wei, D. Jiang, E. B. Ehlerding, T. E. Barnhart, Y. Yang, J. W. Engle, Q. Y. Luo, P. Huang, W. Cai, *Adv Sci (Weinh).* **2019** , *6* , 1801237.[18] M. Nollet, J. Stalin, A. Moyon, W. Traboulsi, A. Essaadi, S. Robert, N. Malissen, R. Bachelier, L. Daniel, A. Foucault-Bertaud, C. Gaudy-Marqueste, R. Lacroix, A. S. Leroyer, B. Guillet, N. Bardin, F. Dignat-George, M. Blot-Chabaud, *Oncotarget.* **2017** , *8* , 112283.[19] R. Hernandez, H. Sun, C. G. England, H. F. Valdovinos, T. E. Barnhart, Y. Yang, W. Cai, *Mol Pharm.* **2016** , *13* , 2563.[20] Y. Yang, R. Hernandez, J. Rao, L. Yin, Y. Qu, J. Wu, C. G. England, S. A. Graves, C. M. Lewis, P. Wang, M. E. Meyerand, R. J. Nickles, X. W. Bian, W. Cai, *Proc Natl Acad Sci U S A.* **2015** , *112* , E6525.[21] C. G. England, D. Jiang, R. Hernandez, H. Sun, H. F. Valdovinos, E. B. Ehlerding, J. W. Engle, Y. Yang, P. Huang, W. Cai, *Mol Pharm.* **2017** , *14* , 3239.[22] H. Sun, C. G. England, R. Hernandez, S. A. Graves, R. L. Majewski, A. Kamkaew, D. Jiang, T. E. Barnhart, Y. Yang, W. Cai, *Eur J Nucl Med Mol Imaging.* **2016** , *43* , 2169.[23] R. Hernandez, H. Sun, C. G. England, H. F. Valdovinos, E. B. Ehlerding, T. E. Barnhart, Y. Yang, W. Cai, *Theranostics.* **2016** , *6* , 1918.[24] C. A. Ferreira, L. Kang, C. Li, A. Kamkaew, K. E. Barrett, E. Aluicio-Sarduy, Y. Yang, J. W. Engle, D. Jiang, W. Cai, *Am. J. Cancer Res.* **2021** , *11* , 1586.[25] C. Li, L. Kang, K. Fan, C. A. Ferreira, K. V. Becker, N. Huo, H. Liu, Y. Yang, J. W. Engle, R. Wang, X. Xu, D. Jiang, W. Cai, *Bioconjug Chem.* **2021** , *32* , 1306.[26] Y. Chen, X. Hou, D. Li, J. Ding, J. Liu, Z. Wang, F. Teng, H. Li, F. Zhang, Y. Gu, S. Yu, X. Qian, Z. Yang, H. Zhu, *J Pharm Anal.* **2023** , *13* , 367.[27] Y. Luo, H. Duan, Y. Qian, L. Feng, Z. Wu, F. Wang, J. Feng, D. Yang, Z. Qin, X. Yan, *Cell Res.* **2017** , *27* , 352.[28] H. Duan, L. Jing, J. Xiang, C. Ju, Z. Wu, J. Liu, X. Ma, X. Chen, Z. Liu, J. Feng, X. Yan, *Adv Sci (Weinh).* **2022** , *9* , e2103719.[29] H. Duan, S. Zhao, J. Xiang, C. Ju, X. Chen, I. Gramaglia, X. Yan, *Cell. Mol. Immunol.* **2021** , *18* , 2443.[30] B. Chan, S. Sinha, D. Cho, R. Ramchandran, V. P. Sukhatme, *Dev Dyn.* **2005** , *232* , 232.[31] Z. Ali, N. Yousaf, J. Larkin, *EJC Suppl.* **2013** , *11* , 81.[32] M. Mihajlovic, S. Vljakovic, P. Jovanovic, V. Stefanovic, *Int J Clin Exp Pathol.* **2012** , *5* , 739.[33] J. Shi, T. Jiao, Q. Guo, W. Weng, L. Ma, Q. Zhang, L. Wang, J. Zhang, C. Chen, Y. Huang, M. Wang, R. Pan, Y. Tang, W. Hu, T. Meng, S. H. Liu, J. Guo, Y. Kong, X. Meng, *Cancer Res.* **2023** .[34] P. Wang, Y. Qu, C. Li, L. Yin, C. Shen, W. Chen, S. Yang, X. Bian, D. Fang, *Int J Nanomedicine.* **2015** , *10* , 749.[35] D. S. Abou, T. Ku, P. M. Smith-Jones, *Nucl. Med. Biol.* **2011** , *38* , 675.[36] S. Y. Cho, E. J. Lipson, H. J. Im, S. P. Rowe, E. M. Gonzalez, A. Blackford, A. Chirindel, D. M. Pardoll, S. L. Topalian, R. L. Wahl, *J. Nucl. Med.* **2017** , *58* , 1421.[37] D. Liu, Du L, D. Chen, Z. Ye, H. Duan, T. Tu, J. Feng, Y. Yang, Q. Chen, X. Yan, *Oncotarget.* **2016** , *7* , 40704.

# Graphical Abstract



$^{89}\text{Zr}$ -IP150 can be used to image various CDXs of humanized melanoma, and for the first time, the clinical conversion potential of  $^{89}\text{Zr}$ -IP150 was explored using a more clinically representative melanoma PDX model.

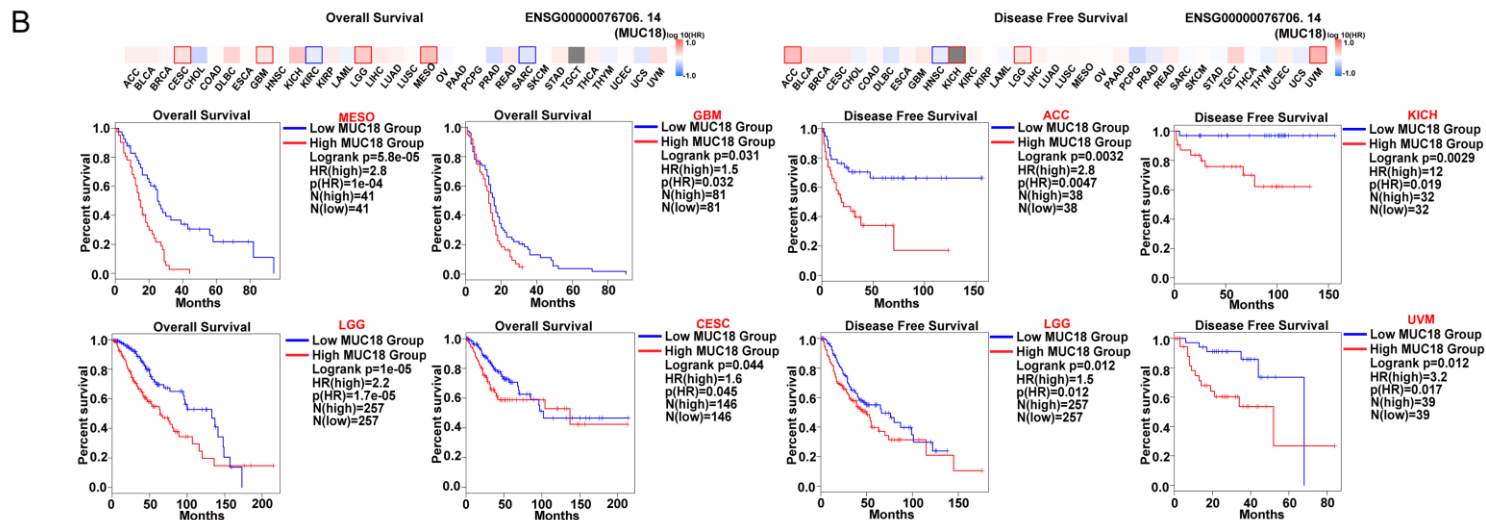
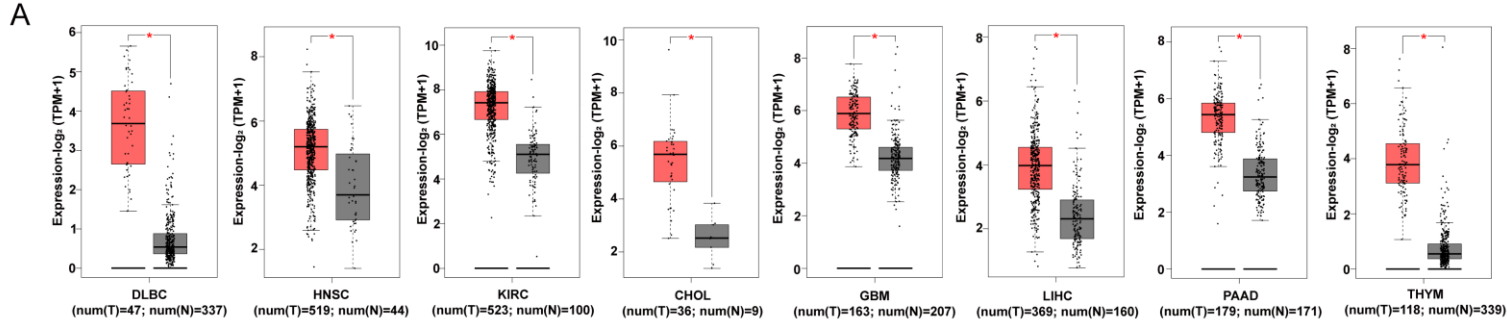


**Figure 1.** Analysis of GEPIA2 outputs. **(A)** Comparisons of MUC18 expression levels between tumor and non-tumor control tissues (The expression levels showed significant difference between tumor and non-tumor); red, expression levels of tumor, black, expression levels of non-tumor; \*,  $p < 0.05$ . **(B)** The prognostic impacts of MUC18 expression level based on the survival heat map. The heat map shows the hazard ratios in logarithmic scale ( $\log_{10}$ ) for MUC18. The red and blue blocks denote higher and lower risks, respectively. The rectangles with red frames mean the significant unfavorable results in prognostic analyses.

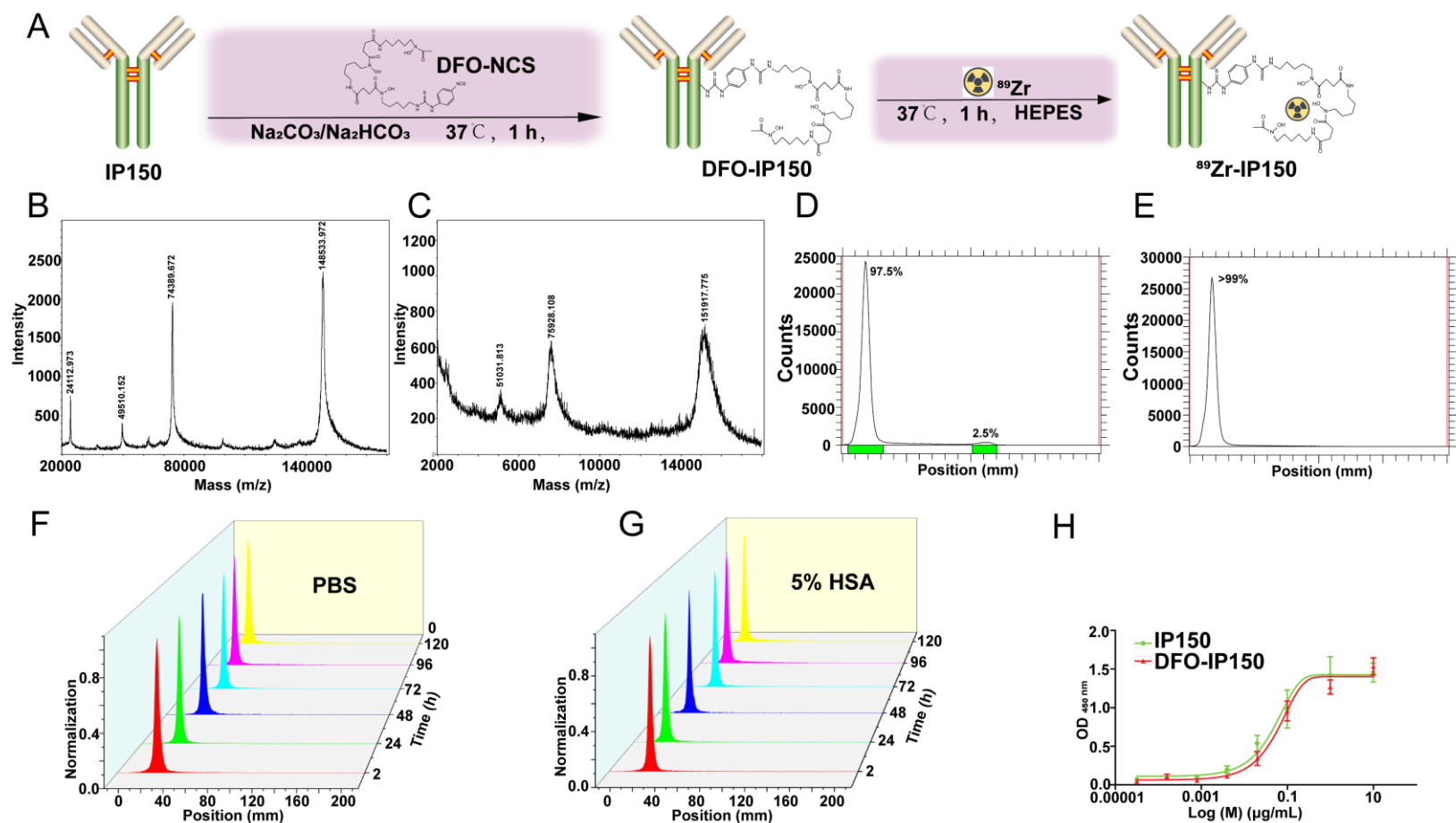


**Figure 2.** (A) Scheme of the  $^{89}\text{Zr}$ -labeled IP150. (B), (C) Average molecular weight of IP150 and DFO-IP150 as measured by MALDI-TOF-MS. (D) (E) The radiochemical purity of unpurified/purified  $^{89}\text{Zr}$ -IP150. (F), (G) In vitro stability analysis of  $^{89}\text{Zr}$ -IP150 over time in 0.01 M pH 7.4 PBS and 5% HSA at RT. (H) Comparison of the binding ability of IP150 and DFO-IP150 to the MUC18 protein by ELISA assay.

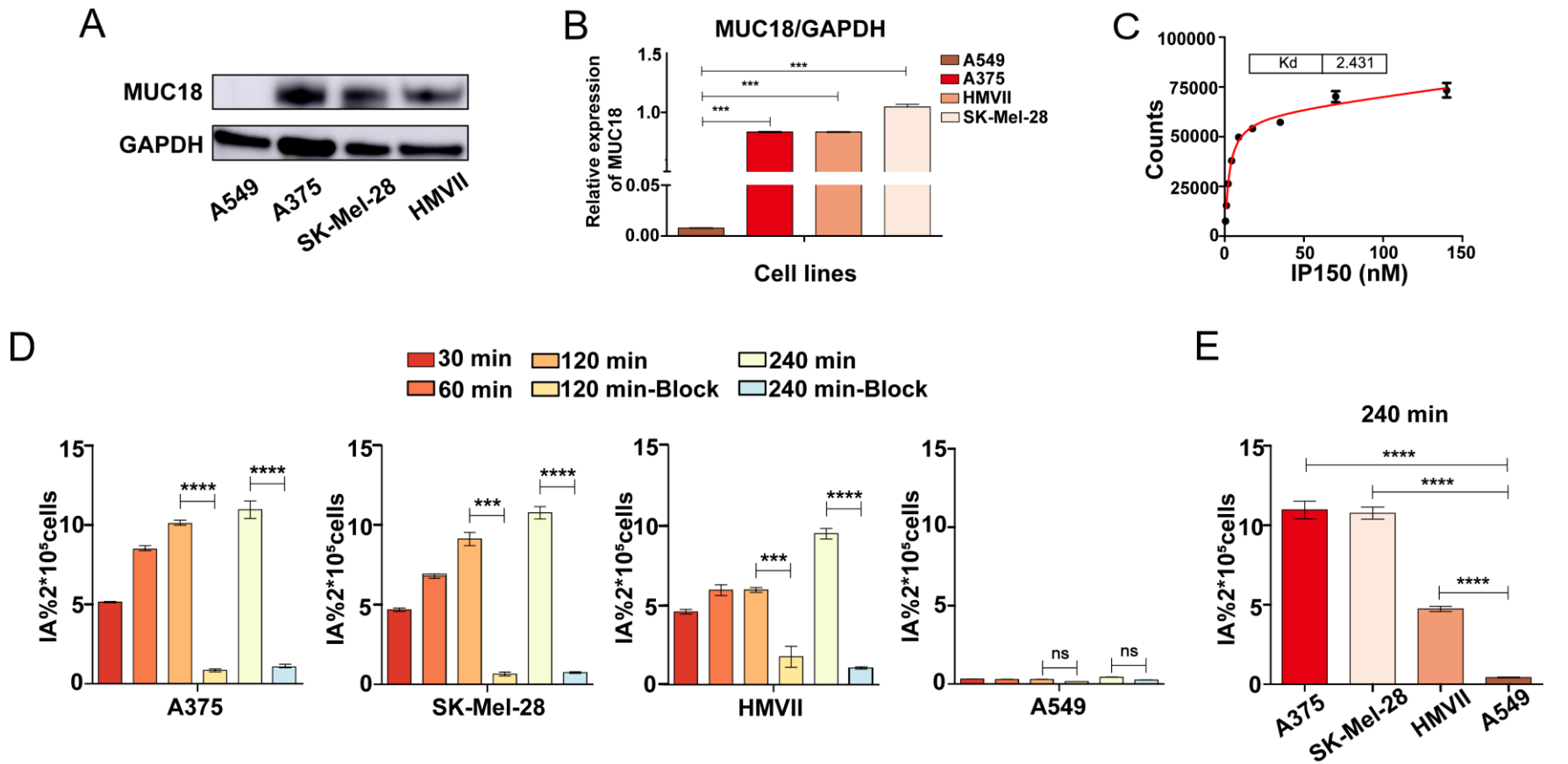


**Figure 3.** (A) (B) Protein expression levels of MUC18 in different human melanoma cell lines and human lung cancer cell. (C) Receptor binding assay of  $^{89}\text{Zr}$ -IP150 in A375 cell line. (D) Cellular uptake of  $^{89}\text{Zr}$ -IP150 in A375, SK-Mel-28 (cutaneous melanoma), HMVII (mucosal melanoma). (E) Comparison of the uptake in four cell lines at 240 min. \*\*\*,  $p < 0.001$ ; \*\*\*\*,  $p < 0.0001$ .

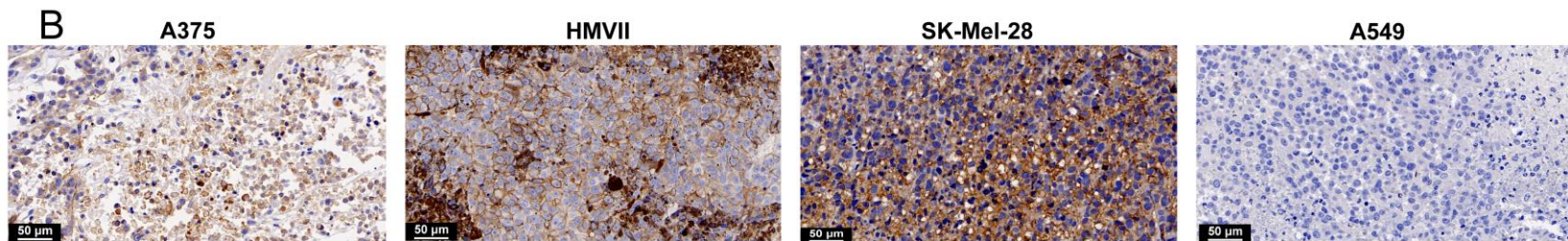
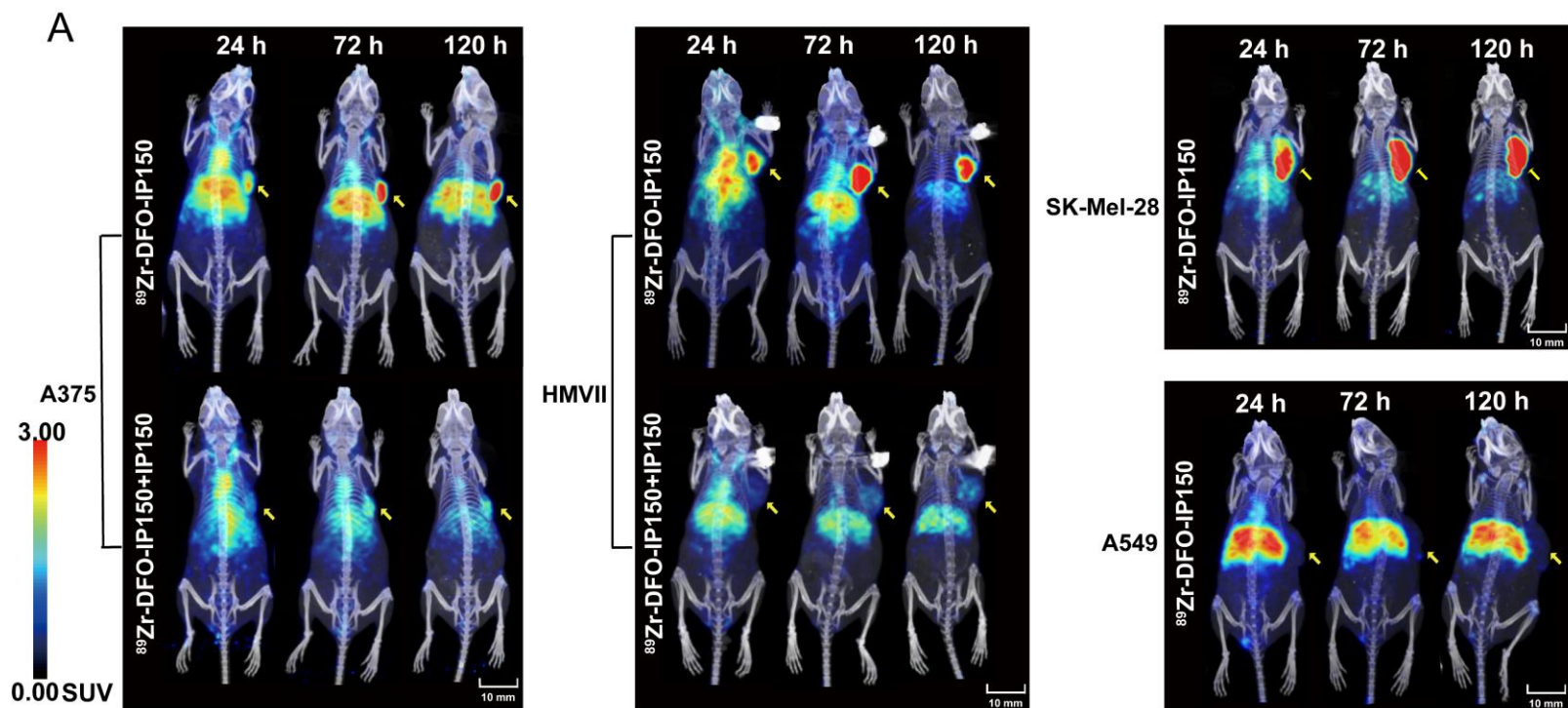


**Figure 4. (A)** Micro-PET/CT images of A375 tumor-bearing mice acquired 24, 72 and 120 hours after administration of  $^{89}\text{Zr-IP150}$  (80  $\mu\text{Ci}$ , 15  $\mu\text{g}$ , in 200  $\mu\text{L}$  PBS) via tail-vein injections ( $n = 3/\text{group}$ ). **(B)** IHC staining of MUC18 in A375, HMVII, SK-Mel-28 and A549.

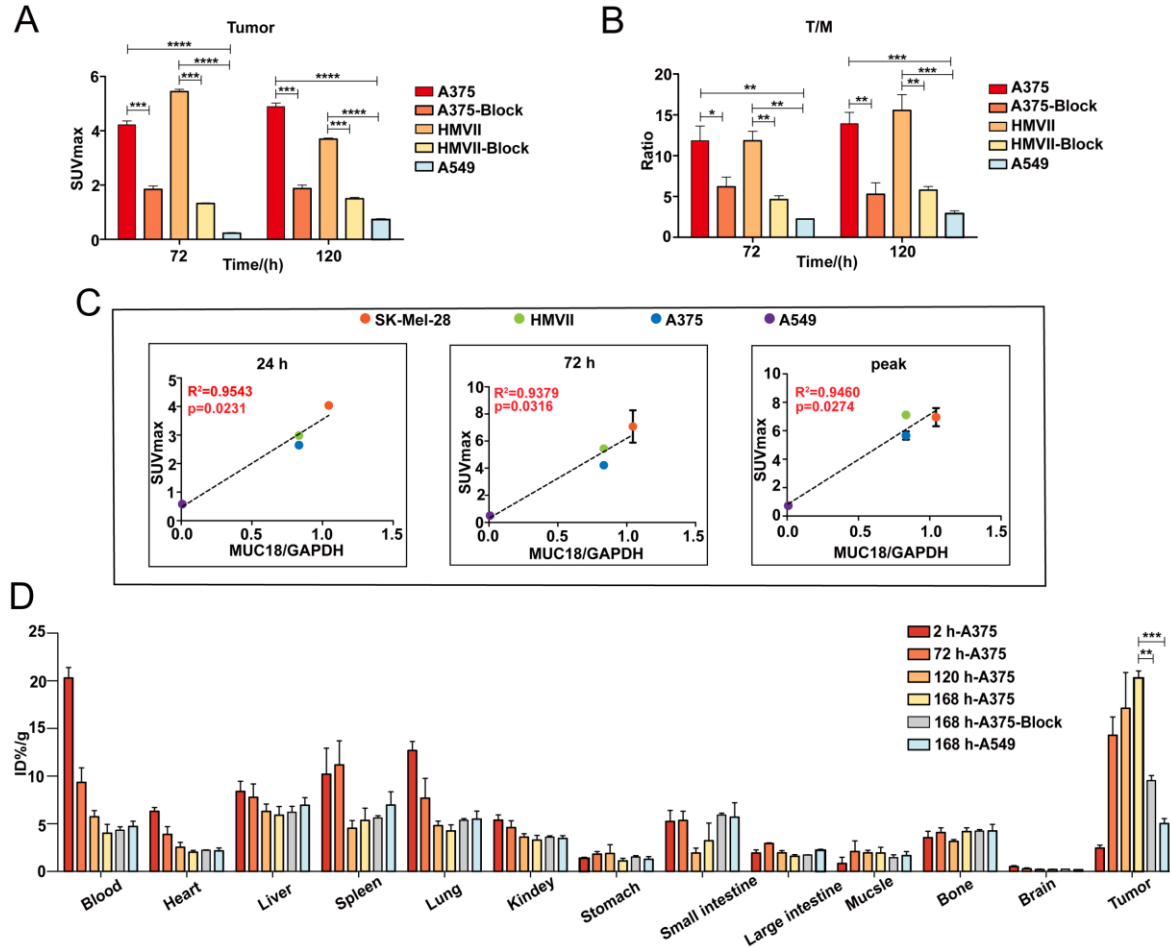


**Figure 5.** (A) (B) Region of interest (ROI) analysis of the PET images. values are presented as SUVmax (n = 3). (C) Correlation analysis between SUVmax value and CD146 expression. (D) Ex-vivo biodistributions of A375 and A549 models at 2 h, 72 h, 120 h and 168 h p.i. (n = 3/group). \*,  $p < 0.05$ ; \*\*,  $p < 0.01$ ; \*\*\*,  $p < 0.001$ ; \*\*\*\*,  $p < 0.0001$ .

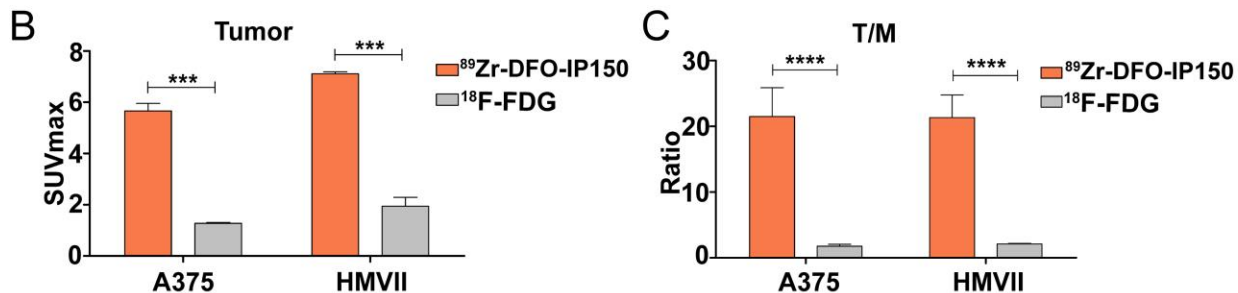
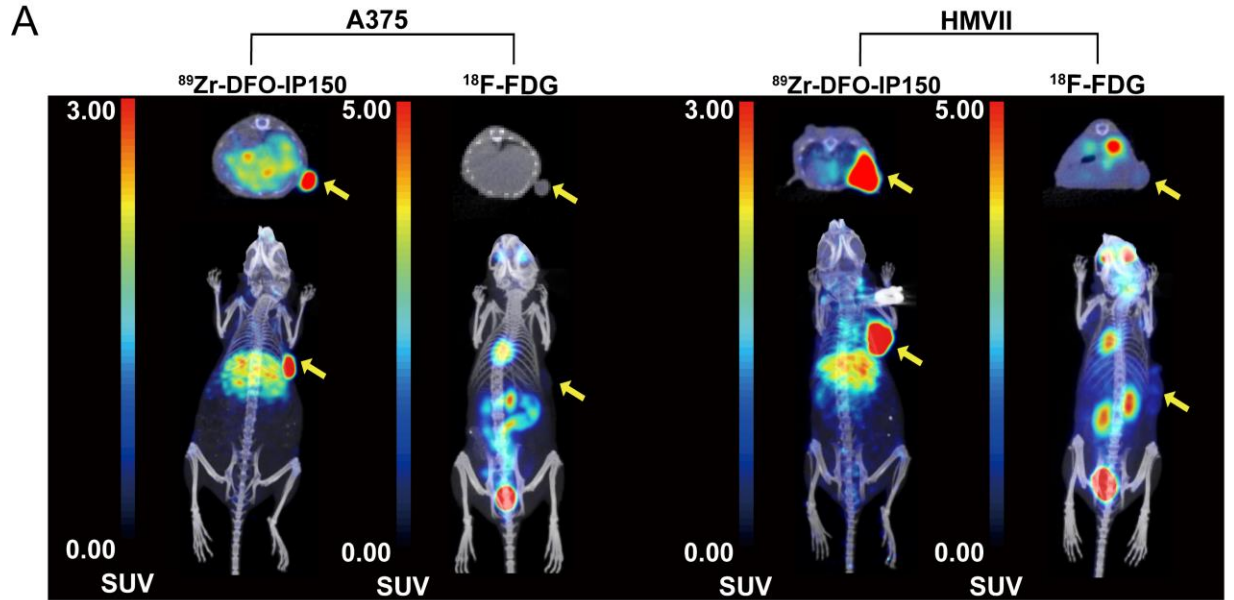


**Figure 6.** (A) Comparison of the Micro-PET/CT images of A375, HMVII tumor-bearing mice after administration of  $^{89}\text{Zr-IP150}$  (80  $\mu\text{Ci}$ , 15  $\mu\text{g}$ , in 200  $\mu\text{L}$  PBS) and  $^{18}\text{F-FDG}$  via tail-vein injections ( $n = 3/\text{group}$ ). (B), (C) ROI and tumor/muscle ratio analysis of the PET images. values are presented as SUVmax( $n = 3$ ). \*\*\*,  $p < 0.001$ ; \*\*\*\*,  $p < 0.0001$ .

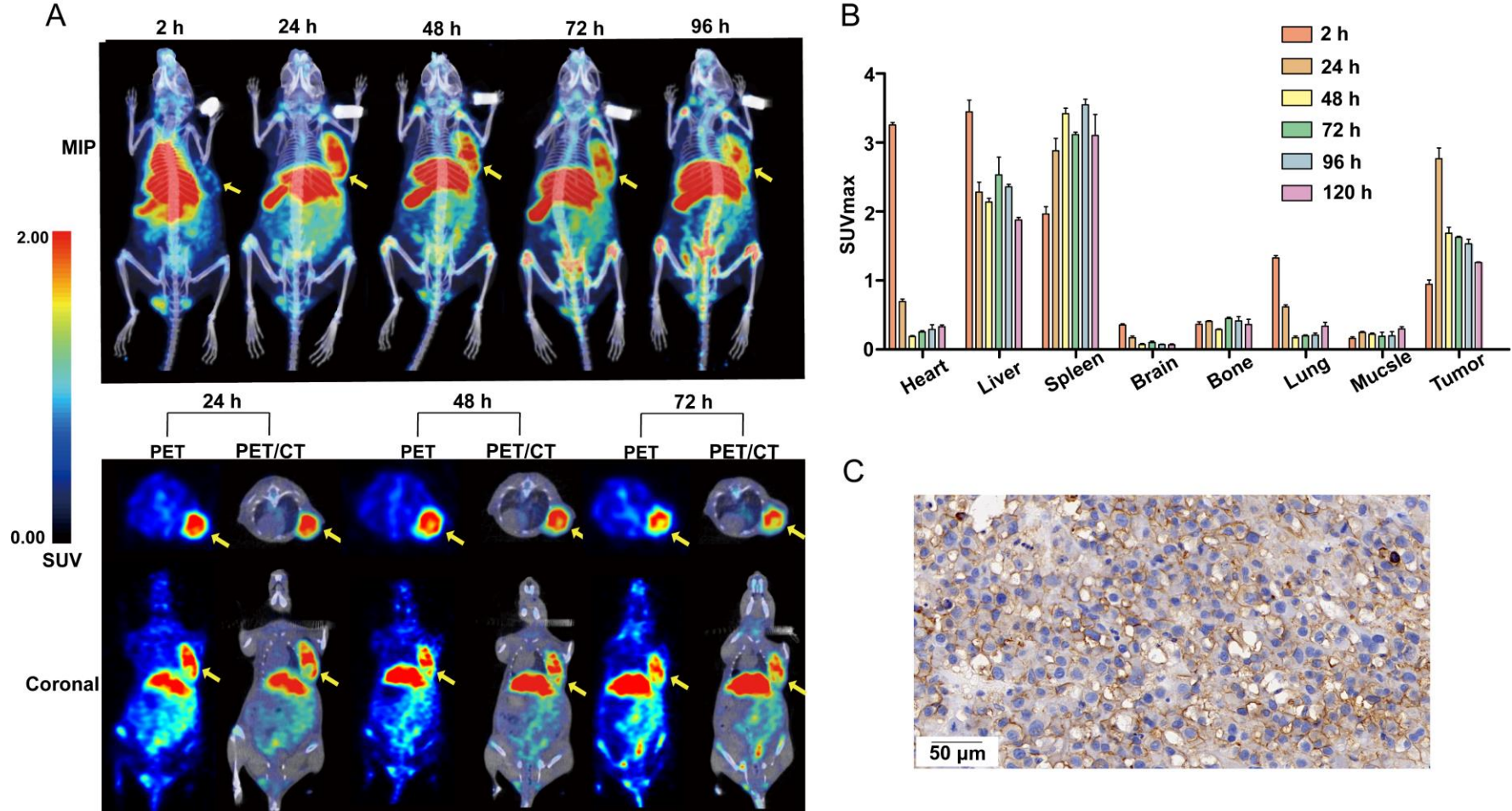


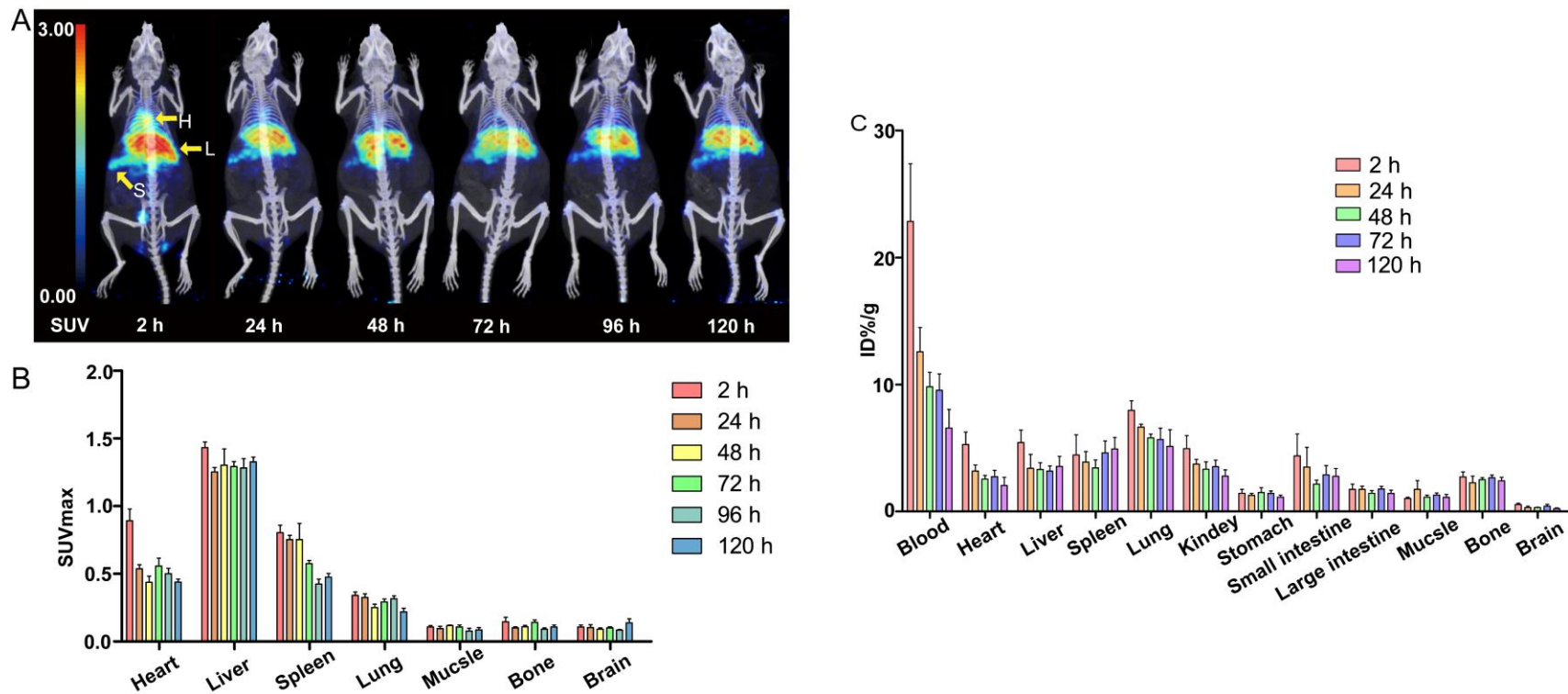
**Figure 7.** (A) MIP images and Coronal images of human melanoma PDX model (acrak lentiginous), after administration of  $^{89}\text{Zr}$ -IP150 (80  $\mu\text{Ci}$ , 15  $\mu\text{g}$ , in 200  $\mu\text{L}$  PBS) via tail-vein injections ( $n = 3/\text{group}$ ). (B) ROI analysis of the PET images, values are presented as SUVmax( $n = 3$ ). (C) IHC staining of MUC18 in PDX model.

**Table 1.** Quality Control of  $^{89}\text{Zr}$ -IP150

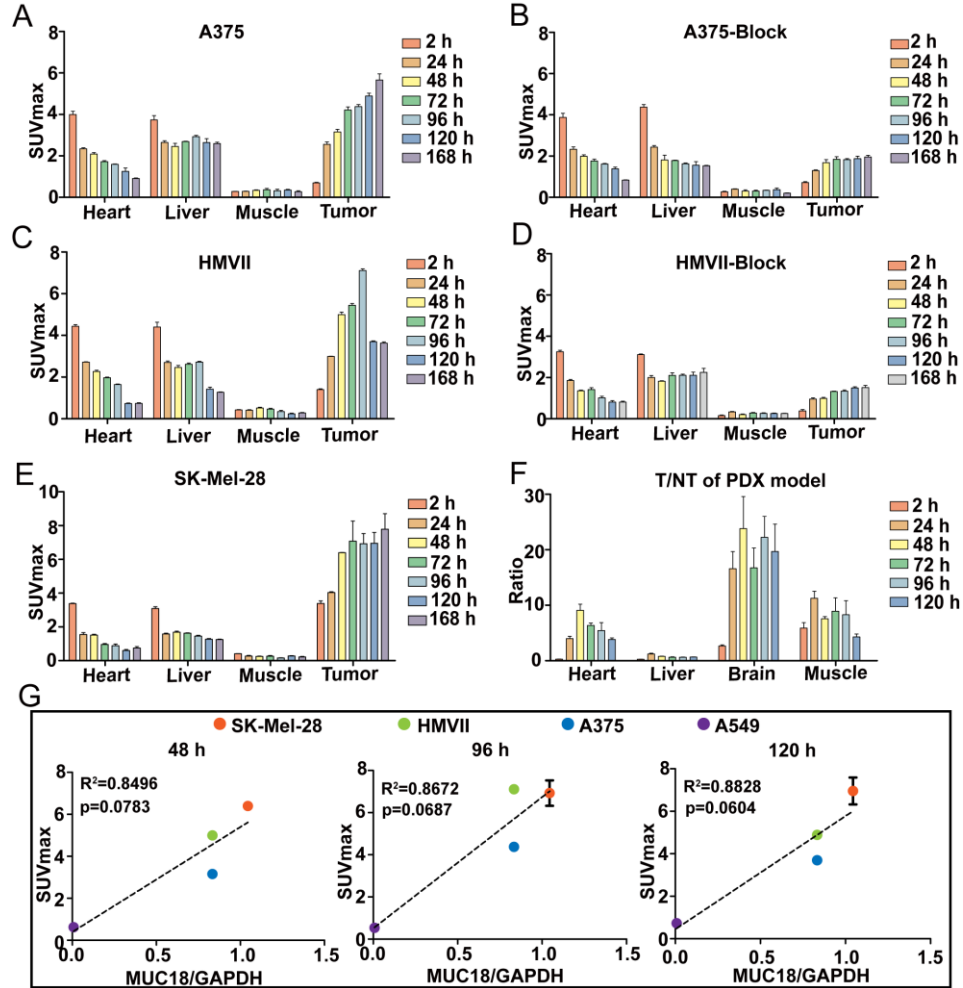
Parameters	Quality Control Specification	Quality Control Result
Appearance	Clear, colorless	Clear, colorless
Volume	1-2 mL	1.5 mL
pH	5.0-8.0	7.4
Radiochemistry purity (iTLC)	> 95%	>99%
Ethanol	<5%	Pass
Endotoxins	< 15 EU/mL	Pass
Sterility	Sterile	Pass
Specific activity (GBq/ $\mu\text{mol}$ )	18.5 – 296.0 GBq/ $\mu\text{mol}$	28.22 $\pm$ 8.53

**Table 2.** Human Organ Radiation Dosimetry Estimation of  $^{89}\text{Zr}$ -IP150 in Adult Female Patients Using OLINDA/EXM 1.0

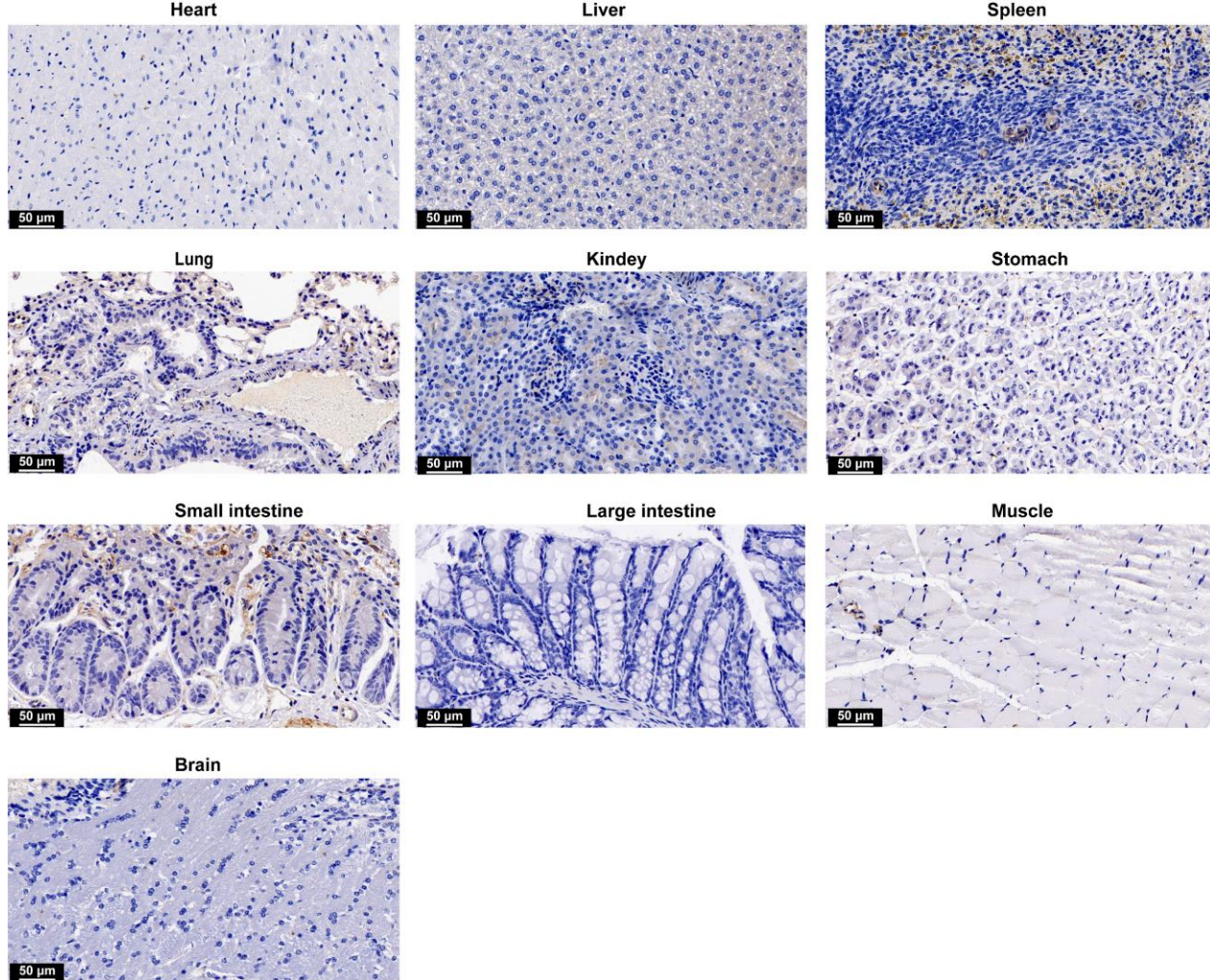
Target Organ	Total (mGy/MBq)
Adrenals	1.10E-01
Brain	6.99E-02
Breasts	2.25E-02
Esophagus	7.22E-02
Eyes	1.69E-02
Gallbladder Wall	6.38E-02
Left colon	3.48E-02
Small Intestine	1.23E-01
Stomach Wall	5.47E-02
Right colon	3.22E-02
Rectum	6.37E-02
Heart Wall	1.08E-01
Kidneys	1.17E-01
Liver	2.18E-01
Lungs	1.95E-01
Ovaries	1.73E-02
Pancreas	6.73E-02
Salivary Glands	1.66E-02
Red Marrow	3.14E-02
Osteogenic Cells	3.71E-02
Spleen	2.11E-01
Thymus	6.37E-02
Thyroid	3.19E-02
Urinary Bladder Wall	1.25E-02
Uterus	2.48E-02
Total Body	3.02E-02
Effective Dose(mSV/MBq)	6.45E-02



**Supplementary Figure 1.** (A) Micro-PET/CT images of KM mice after administration of  $^{89}\text{Zr}$ -IP150 (80  $\mu\text{Ci}$ , 15  $\mu\text{g}$ , in 200  $\mu\text{L}$  PBS) via tail-vein injections ( $n = 3/\text{group}$ ). (B) ROI analysis of the PET images, values are presented as SUVmax ( $n = 3$ ). (C) Ex vivo biodistributions of KM mice at 2 h, 24 h, 48 h, 72 h and 120 h p.i. ( $n = 3/\text{group}$ ).



**Supplementary Figure 2.** (A) (B) (C) (D) (E) ROI analysis of the PET images. (F) T/NT of PDX models. values are presented as SUVmax (n = 3). (G) Correlation analysis between SUVmax value at 48, 96, 120 h and MUC18 expression.



**Supplementary Figure 3.** IHC staining of MUC18 in normal tissues of PDX model.